

POLITECNICO DI MILANO
Facoltà di Ingegneria dei Processi Industriali
Degree in Materials Engineering and Nanotechnology



ATOMIC LAYER DEPOSITION OF
FERROELECTRIC COMPLEX
OXIDE THIN FILMS

Advisor Dr. Jonathan E. Spanier

Drexel University, Philadelphia, Pennsylvania, United States of America

Co-Advisor Dr. Carlo S. Casari

Politecnico di Milano, Milano, Italia

A THESIS
Submitted to the Faculty in
PARTIAL FULFILLMENT
of the Requirements
for the Degree of
MASTER OF SCIENCE
by:

Brian R. Beatty

Matricola: 780703

Academic Year 2011-2012

© Copyright August 2012
Brian R. Beatty. All Rights Reserved.

For my parents...

Contents

List of Figures	vi
List of Tables	vii
Acknowledgements	ix
5 Abstract	xi
Sommario	xiii
1 Introduction	1
1.1 Project Scope	1
2 Lead Titanate	3
10 2.1 Structure	3
2.1.1 Effect of Temperature	4
2.2 Ferroelectricity	4
3 Synthesis Methods	7
15 3.1 Sol-Gel Processing	7
3.2 Metallorganic Chemical Vapor Deposition	7
3.3 Atomic Layer Deposition	7
4 Characterization Methods	11
20 4.1 Compositional Analysis	11
4.1.1 Energy-Dispersive X-Ray Spectroscopy	11
4.1.2 X-Ray Fluorescence Spectroscopy	11
4.2 Thin Film Characterization	12
4.2.1 Variable Angle Spectroscopic Ellipsometry	12
4.3 Phase Identification	15
4.3.1 X-Ray Diffraction	15
4.3.2 Grazing Incidence X-Ray Diffraction	17
25 4.4 Thermal Analysis	17
4.4.1 Thermogravimetric Analysis	17
4.4.2 Differential Scanning Calorimetry	18

5 Sample Fabrication	21
30 5.1 Precursor Selection	21
5.1.1 Titanium Source	21
5.1.2 Lead Source	21
5.1.3 Oxidizer	21
35 5.2 Substrate Preparation	22
5.2.1 Si(100)	22
5.2.2 Platinized Si(100)	22
5.2.3 STO(100) and Nb:STO(100)	23
40 5.3 Deposition Parameters	23
5.3.1 Growth Temperature	23
5.3.2 Precursor Dosage	24
5.3.3 Purge Time	25
5.3.4 Exposure Time	25
45 5.4 Post-Deposition Annealing	25
5.4.1 Oven Annealing	26
5.4.2 Rapid Thermal Annealing	26
6 Data Collection and Analysis	27
50 6.1 Thermal Analysis	27
6.1.1 Thermogravimetric Analysis	27
6.1.2 Differential Scanning Calorimetry	27
6.2 VASE and Modeling	27
6.2.1 Data Collection	27
6.2.2 Model Definition	28
6.2.3 Analysis Procedure	29
6.3 Composition Analysis	32
6.3.1 X-Ray Fluorescence Spectroscopy	33
6.4 X-Ray Diffraction	33
6.4.1 Grazing Incidence XRD	33
7 Results	35
60 7.1 Thermal Analysis	35
7.1.1 Thermogravimetric Analysis	35
7.1.2 Differential Scanning Calorimetry	36
7.2 Ellipsometry	36
7.3 Composition	36

65	7.4 X-Ray Diffraction	36
65	8 Conclusions	37
70	8.1 Future Work	37
75	Bibliography	39
75	A Supplemental Information	41
75	A.1 List of Chemicals	41
75	A.2 List of Samples	42
75	A.3 ALD Reactor Diagram	43
75	A.4 Recipes for S100 ALD System	44
75	A.5 Thermal Analysis Results	45
75	A.5.1 Thermogravimetric Analysis	45
75	A.5.2 Differential Scanning Calorimetry	48
75	A.6 Composition Results	50
75	A.7 Ellipsometry Results	52
75	A.8 XRD Results	59

List of Figures

80	2.1 Crystal Structures of Perovskites and PbTiO ₃	3
	2.2 Energy vs. Polarization Plots for FE and PE Materials	5
	2.3 Polarization vs. Applied Field Plots for FE and PE Materials . .	5
	3.1 Illustration of Example ALD Cycle	8
85	4.1 Illustration of EDXS principle	12
	4.2 Ellipsometric Beam Path and Modeling Parameters	13
	4.3 J.A. Woollam M-2000U Ellipsometer	15
	4.4 Illustration of Bragg's Law	16
	(a) Constructive Interference	16
	(b) Destructive Interference	16
90	4.5 Brüker D8 Discover XRD	17
	4.6 Rigaku SmartLab XRD	18
	4.7 T.A. Instruments, inc. Instrumentation	19
	(a) Q50 TGA	19
	(b) Q2000 DSC	19
95	6.1 Graphical Schematic of VASE Model	29
	6.2 Preferred Phase vs. Stoichiometric Ratio	33
	A.1 Cambridge NanoTech, inc. S100 ALD System	43
	(a) Photograph	43
	(b) Schematic Diagram	43
100	A.2 TGA Results for Pb(HFAC) ₂ Precursor	45
	(a) Mass vs. Temperature	45
	(b) Derivative of Mass vs. Temperature	45
	A.3 TGA Results for Pb(HFAC) ₂ Precursor	46
	(a) Mass vs. Temperature	46
105	(b) Derivative of Mass vs. Temperature	46
	A.4 Constant Temperature TGA Experiments	47
	(a) Pb(HFAC) ₂	47
	(b) Pb(TMHD) ₂	47
	A.5 Results of DSC Experiments	49
110	(a) Pb(HFAC) ₂	49
	(b) Pb(TMHD) ₂	49

A.6	XRF Spectrum of PTO #0	51
A.7	XRF Spectrum of PTO #20 on Pt-Si	51
A.8	Results of Ellipsometry on Sample #0	53
115	(a) Psi vs. Wavelength	53
	(b) Delta vs. Wavelength	53
	(c) n, k vs. Photon Energy	53
A.9	Results of Tauc Analysis on Sample #0	54
120	(a) Absorption (α) vs. Photon Energy	54
	(b) Tauc ($\alpha^2 E_{ph}^2$) vs. Photon Energy	54
A.10	Results of Ellipsometry on Sample #20 on Platinized Silicon	55
	(a) Psi vs. Wavelength	55
	(b) Delta vs. Wavelength	55
	(c) n, k vs. Photon Energy	55
125	A.11 Results of Tauc Analysis on Sample #20 on Platinized Silicon	56
	(a) Absorption (α) vs. Photon Energy	56
	(b) Tauc ($\alpha^2 E_{ph}^2$) vs. Photon Energy	56
A.12	Results of Ellipsometry on Sample #28 on STO	57
130	(a) Psi vs. Wavelength	57
	(b) Delta vs. Wavelength	57
	(c) n, k vs. Photon Energy	57
A.13	Results of Tauc Analysis on Sample #28 on STO	58
	(a) Absorption (α) vs. Photon Energy	58
	(b) Tauc ($\alpha^2 E_{ph}^2$) vs. Photon Energy	58
135	A.14 Results of XRD Experiments on Sample #20 on Platinized Silicon	59
	(a) Full Range	59
	(b) PTO (100) and PbO ₂	59
	(c) PbO (220) and PTO (200)	59

List of Tables

140	A.1 List of Samples	42
	A.2 XRF Calculated Compositions	50
	A.3 PTO #0 Ellipsometric Model Variables	52
	A.4 PTO #20 Ellipsometric Model Variables	52
	A.5 PTO #28 Ellipsometric Model Variables	54
145	A.6 Calculated Band Gap Energies	55

Acknowledgements

Dr. Jonathan Spanier

Eric Gallo, Dr. Maria Sancho-Torres, Dr. Stephen Nonenmann, Stephanie Johnson, Oren Leaffer, Terrence McGuckin, Guannan Chen, Christopher Hawley

150 Keith Fahnestock and Professor Caroline Schauer

Rahul Joseph, Dr. Greg Soja

Dr. Amy Peterson and Professor Giuseppe Palmese

Other Professors in MATE dept. and Drexel University

155 Dr. Carlo Casari, as well as Politecnico di Milano

Family and friends.

Abstract

Comments on application of ferroelectric materials.

As devices based on ferroelectric films become more commonplace, a commercially viable process for fabricating the material is needed; low cost and high volume are implied necessities for such a process. This work focuses on the application of atomic layer deposition (ALD) to this task. ALD is a standard fabrication process in the electronics industry, valuable for its high uniformity across large surfaces, capability to control film thickness with very high resolution, and conformality across three dimensional structures. The various tasks in designing and optimizing an ALD process, as well as characterization methods for analysis of the produced films, are discussed here in detail.

The primary focus of this work is the development of a process for depositing lead titanate ($PbTiO_3$) thin films via an ALD process. Research focused on the application of bis(2,2,6,6-tetramethyl-3,5-heptanedionato)lead(II) ($Pb(TMHD)_2$) toward this end.

Work supported by ARO under Grant #??.

Sommario

A detailed summary of the document to be presented solely in Italian.

¹⁷⁵ **Chapter 1**

Introduction

1.1 Project Scope

The primary scope of this project involved the creation of a method to produce lead titanate thin films. To this end, a number of different steps
¹⁸⁰ needed to be taken. Primarily,

Chapter 2

Lead Titanate

2.1 Structure

Lead titanate (PbTiO_3 , PTO) naturally orders into the tetragonal perovskite crystal structure at room temperature (figure 2.1). The structure can be affected by compositional changes, temperature, or strain (primarily in thin-film systems), allowing a transition to a cubic phase. In the perovskite crystal structure, the central cation (Ti^{4+} in the case of PbTiO_3) is encapsulated in a octahedral cage of anions (O^{2-}), with the remaining cations (Pb^{2+}) situated in the eight corners of the unit cell. if the material was doped (as in a mixed solid-solution), some of the cations would be replaced with the dopant ions, for example Zr^{4+} would be randomly distributed in Ti^{4+} sites in the $\text{PbTi}_{1-x}\text{Zr}_x\text{O}_3$ (PZT) system.

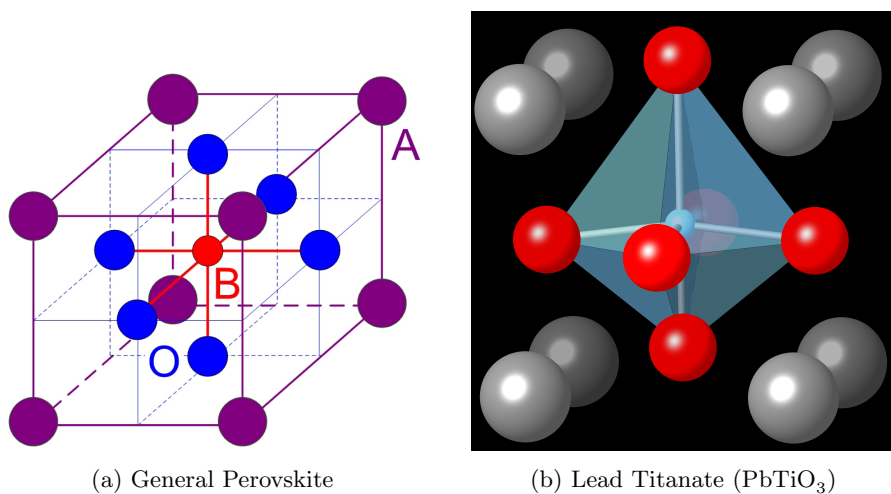


Figure 2.1: The perovskite (ABO_3) crystal structure.

(a) The general structure of perovskite oxides. (b) Tetragonal asymmetric perovskite structure of PbTiO_3 . Grey, red, and blue spheres refer to Pb^{2+} , Ti^{4+} , and O^{2-} , respectively. Additionally, the octahedral oxygen cage is shown in pale blue.

2.1.1 Effect of Temperature

195 The transition from tetragonal to cubic perovskite is highly dependent on temperature. The critical temperature at which this transition occurs is referred to as the Curie temperature (T_C). If the material cools through this temperature, a lengthening of the ‘c’ axis of the unit cell spontaneously occurs via a first order phase transition. This creates anisotropy in the structure
200 and allows for an anisotropic charge distribution to develop. In lead titanate this is caused by the shifting of the titanium ion, along with a slight shift of some of the oxygen ions as well (visible in figure ?? on page ??). Thus, a permanent dipole is created whose magnitude increases as the system cools further from T_C . This permanent dipole allows the system to exhibit ferroelectricity, implying an ability to semi-permanently switch the orientation of the dipole in the material. This switching can be reversed, but this will not occur spontaneously.

2.2 Ferroelectricity

210 Ferroelectricity is the capability of a material to exhibit spontaneous electric polarization that requires external influence, such as an applied electric field, to be reversed. This is different from paraelectric (or even dielectric) materials, where there is no polarization without external field being applied. This can be seen in a plot of energy vs. polarization (fig. 2.2 on the facing page) for the two types of materials. In a ferroelectric material, the energy minima are
215 found at non-zero levels of polarization.

One of the most important effects of ferroelectric behavior is the exhibition of hysteresis in the polarization state of the material. Suboptimal explanations... Because additional energy is required to make the transition from one state to another, the original state endures for some amount of opposing field
220 (see fig. 2.3b on the next page).

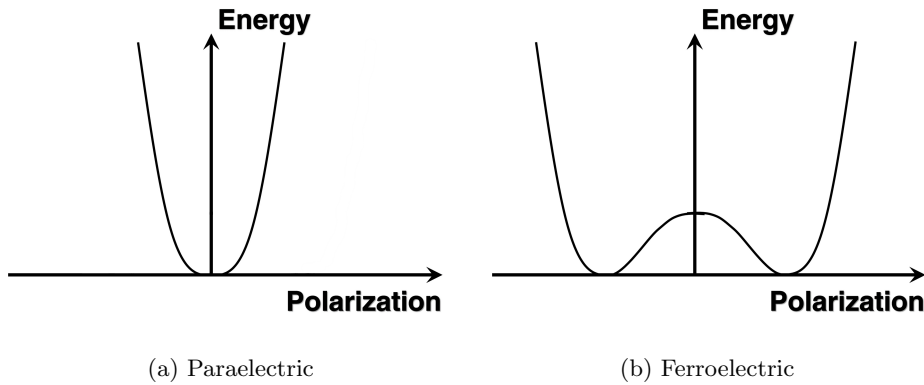


Figure 2.2: Example plots of the energy required to polarize a material. Ferroelectric materials (b) have non-zero polarization at the energy minima. Above T_C all ferroelectric materials transition to a paraelectric phase (a). As temperature increases, the energy minima will approach one another.

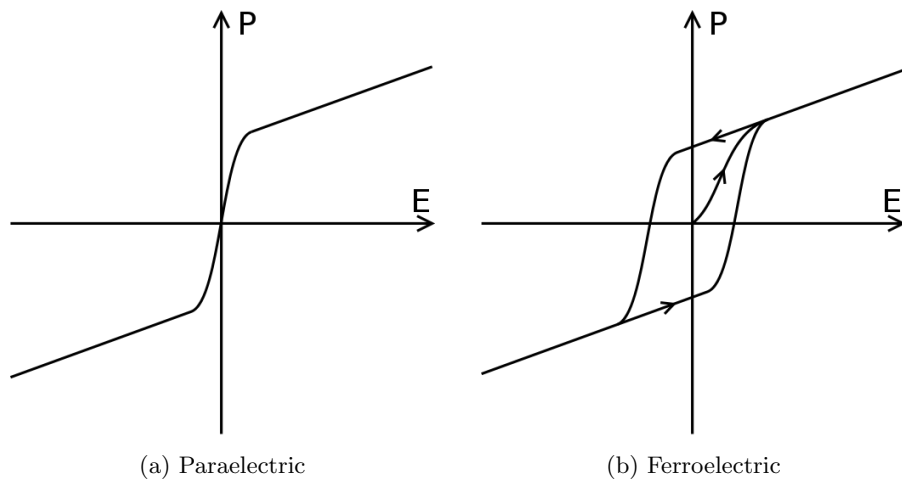


Figure 2.3: Example plots of the polarization as a function of applied field. (a) Paraelectric materials have two regions of polarizability; at low E the polarization increases quickly with the field, as E increases the rate of increase decreases. (b) Ferroelectric materials show similar behavior, but additionally have hysteresis. This means that the films are switchable between two states, but it is difficult to obtain zero polarization.

Chapter 3

Synthesis Methods

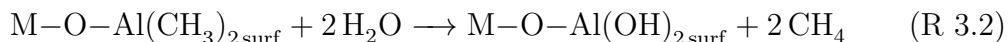
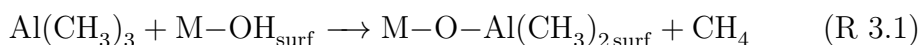
Synthesis of perovskite oxides has been demonstrated using a wide range of techniques. These range from solution-based processing methods (sol-gel approach), to physical vapor methods (molecular beam epitaxy and pulsed laser deposition), and gas phase chemical methods (chemical vapor deposition and atomic layer deposition). This review will briefly discuss sol-gel and CVD methodology, but will focus in more depth on films deposited via ALD.

3.1 Sol-Gel Processing

230 3.2 Metallorganic Chemical Vapor Deposition

3.3 Atomic Layer Deposition

Atomic Layer Deposition (ALD) is a modification on standard CVD processes, with a few major differences. The defining aspect of an ALD process is the separation of the overall reaction into two steps: first the precursor is allowed to react with the substrate surface (see reaction 3.1), excess reactant is purged from the chamber and an oxidizer is introduced to complete the reaction (see reaction 3.2). These reactions show a very simple ALD reaction between trimethylaluminum (TMA, $\text{Al}(\text{CH}_3)_3$) and water.



In this example, it is seen that the first stage allows the TMA to react with the hydrated substrate surface to form part of a layer of alumina (Al_2O_3), liberating a molecule of methane as a byproduct. In the next step, the remaining ligands are stripped away from the bound TMA molecule and replacing them with hydroxyl groups. This returns the system to the initial state — where the surface is presenting sites available to react with more TMA — and the cycle is completed. A graphical example of this process can be found in figure 3.1.

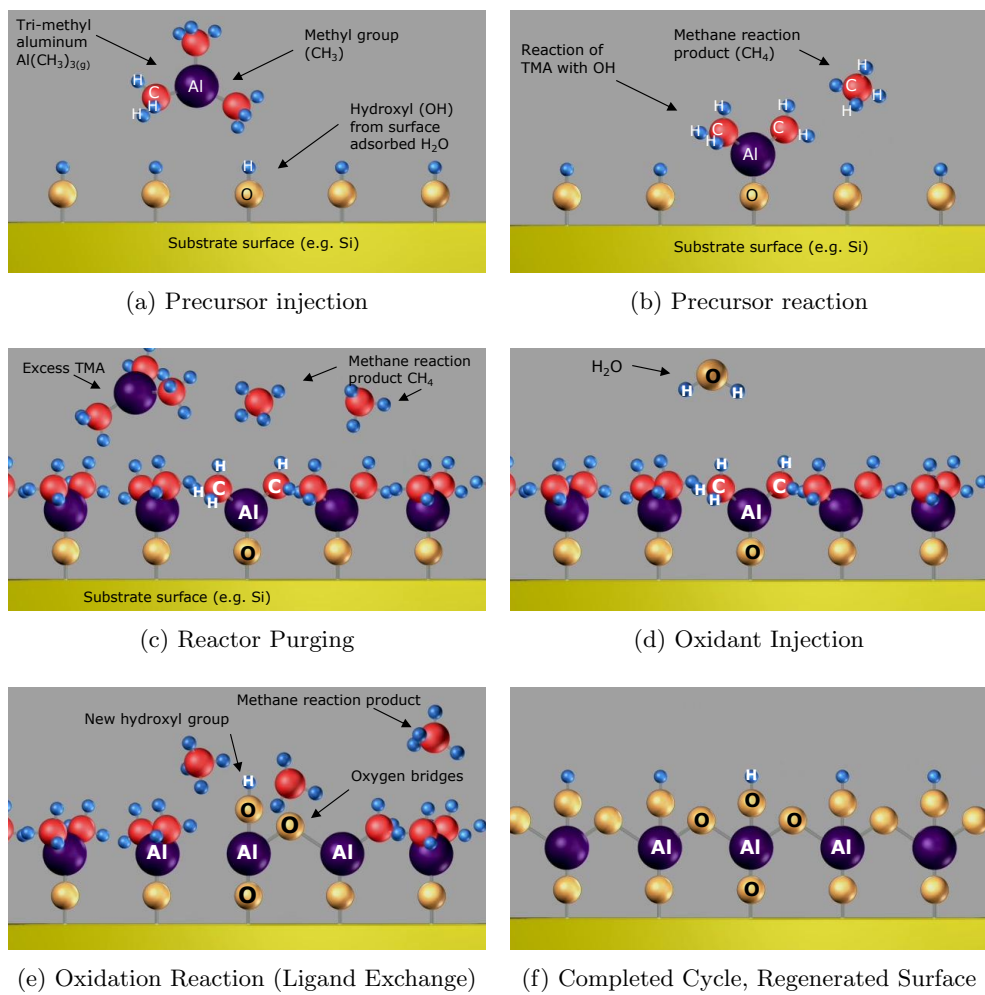


Figure 3.1: Example schematic of the process of an ALD deposition cycle. This example illustrates the reaction of TMA and water to form alumina (Al_2O_3).

Graphic courtesy of Cambridge NanoTech, inc.

Having only surface reactions be permitted, as opposed to CVD where gas-phase interactions dominate, affords ALD a number of unique characteristics. One of these is the concept of the “self-limiting” growth mode. This behavior arises from the limited number of available reaction sites; when all of these have
250 either been reacted with or made unavailable by a blocking mechanism such as stearic hindrance from other local chemisorbed precursor the reaction can no longer proceed. At this point, additional available precursor is not going to be utilized, and instead will be removed and treated as waste material. The system is then evacuated, and a inert purge gas such as dry nitrogen or
255 argon (at UHP grade) is flowed through the reactor. The purge gas serves both to push any remaining gases out of the reactor as well as to help desorb physisorbed species from the surface. If these are allowed to remain adsorbed they would react with the oxidant and negate the surface-limited aspects of ALD. The system would then again be evacuated, and the oxidant introduced
260 and then pumped away to complete the cycle.

In the implementation of most ALD systems, the purge gas is also used as a carrier gas for the precursors. Thus a constant flow of gas is passed through the system, instead of having it occasionally fully evacuated, and the precursor is able to be delivered from its source to the reactor more effectively. For some
265 precursor compounds, in particular those with a low vapor pressure, having carrier-assisted transportation can greatly improve the behavior of the system.

Because of the self-limiting behavior, each deposition cycle is limited to a theoretical maximum of one monolayer of material (in practice a much lower coverage per cycle is attained), which is far less than a unit cell. Generally
270 per cycle growth rates range between 0.03–1.5 Å, with the rate being nearly invariable during most of the deposition. This gives the second defining characteristic of ALD: very high (Å level) thickness resolution. The downside of this aspect is that growths are generally much slower than other types of depositions; ALD is generally slower by an order of magnitude or more than a similar CVD process, as an example. This has proved invaluable in many processes where high precision is critical, such as electronics manufacturing. Intel, for example, uses ALD to deposit extremely thin layers of a high- κ dielectric (such as hafnia, HfO₂) for use as the gate oxide in its transistors, with layer thickness generally less than 2 nm.
275

This method will produce a layer of a binary oxide material (AO_x), if more complex materials are desired the method must be changed. The basic principles remain the same; one would perform the procedure for depositing a
280

cycle of a binary oxide and then change the precursor and deposit another cycle of a different oxide material. For example, if one wished to deposit PbTiO_3 ,
285 one would begin by depositing a layer of TiO_2 and then depositing a layer of lead oxide (PbO). Repeating this set of cycles — a super-cycle — would eventually form the PbTiO_3 film.

However, deposition of complex oxides is not this simple in practice. In many cases, running each oxide cycle in a 1:1 ratio will deposit a non-stoichiometric
290 material. This makes it necessary to modify the method to deposit more of one type of oxide than the other. For example, if a material is Ti-rich the super-cycle ratio would be modified to increase the number of lead oxide cycles as compared to the titania cycles. **Needs more here.**

ALD reactions are rather sensitive to a number of factors, such as temperature.
295 The temperature must be high enough that the reactants have sufficient energy to drive the surface reaction but not so high as to allow undesirable reactions to activate (e.g. precursor cracking or surface material desorption). Precursor selection is also very important, for similar reasons. The precursors must also be incapable of reacting with themselves, to allow the self-limiting
300 mechanism to work properly. **This section needs more work.**

Chapter 4

Characterization Methods

4.1 Compositional Analysis

4.1.1 Energy-Dispersive X-Ray Spectroscopy

305 Energy dispersive X-ray spectroscopy (EDXS) is a commonly used analysis technique for determining the composition of a sample. In this process, a sample is bombarded with high-energy electrons (2–30 keV) which interact with the sample. Some of these electrons will cause a core electron of an atom in the sample to be ejected. This leaves a vacant orbital in the inner shell, which a higher energy electron will fill. In the process of filling the vacancy, the electron will emit an X-ray photon equal to the energy difference between the two states. These energies are referred to using the common X-ray spectroscopy nomenclature (e.g. K_{α} , K_{β} , L_{α}). An illustration of this process can be found in figure 4.1 on the following page.

315 Since the energies of the emitted photons are very specific to each element, the procedure can be used to identify the presence of the element in the sample. With some calibration, EDXS can also be used to quantify the relative amounts of each element in a sample using the different number of collected photons. However, this can sometimes be difficult due to some elements have overlapping 320 spectrums as the peaks are not sharp and different elements can have similar energies for some transitions.

One of the downsides of EDXS is that the interaction volume of electrons is much larger deeper into the sample, so the surface sensitivity of the technique is smaller than with some other techniques.

325

4.1.2 X-Ray Fluorescence Spectroscopy

X-ray fluorescence spectroscopy (XRFS) is a similar technique to EDXS. In XRFS the excitation used is X-ray photons (often from a Cu K_{α} source with $\lambda = 1.54 \text{ \AA}$), as opposed to energetic electrons. In other considerations the techniques are equivalent.

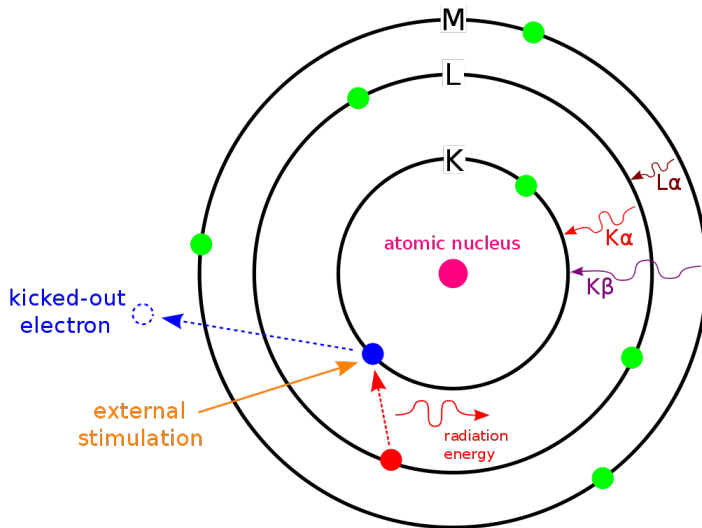


Figure 4.1: Graphic illustrating the basic mechanism for EDXS, along with the commonly used notation for the various energies. The external stimulation would be a high energy electron.

XRFS has a lower noise floor than EDXS, due to the lack of signal from Bremsstrahlung radiation from the deceleration of electrons, allowing smaller signals to be more easily identified (such as in ultra-thin films). It does suffer the same disadvantage of having overlapping peaks. This resolution issue can be alleviated to some degree by using wavelength dispersive XRFS (WD-XRFS), which uses diffraction techniques to analyze the emitted x-ray spectrum.

X-ray fluorescence spectroscopy was performed using a fX-SEM analysis system from iXRF Systems, inc.⁵ It was the primary method of composition analysis for the results presented in this thesis.

4.2 Thin Film Characterization

4.2.1 Variable Angle Spectroscopic Ellipsometry

Ellipsometry is a powerful non-destructive optical technique that allows for the determination of a large number of properties of complex thin film structures. The basic tenet of ellipsometry relies on the analysis of the change in polarization state of a reflected light beam after interaction with the sample. The incident beam is generally linearly polarized, but upon reflection becomes elliptically polarized due to a phase shift in the components of the beam in the s- and p-plane, as well as a change in their relative amplitudes. The phase shift is correlated to the ellipsometric parameter Δ , while the amplitude change is

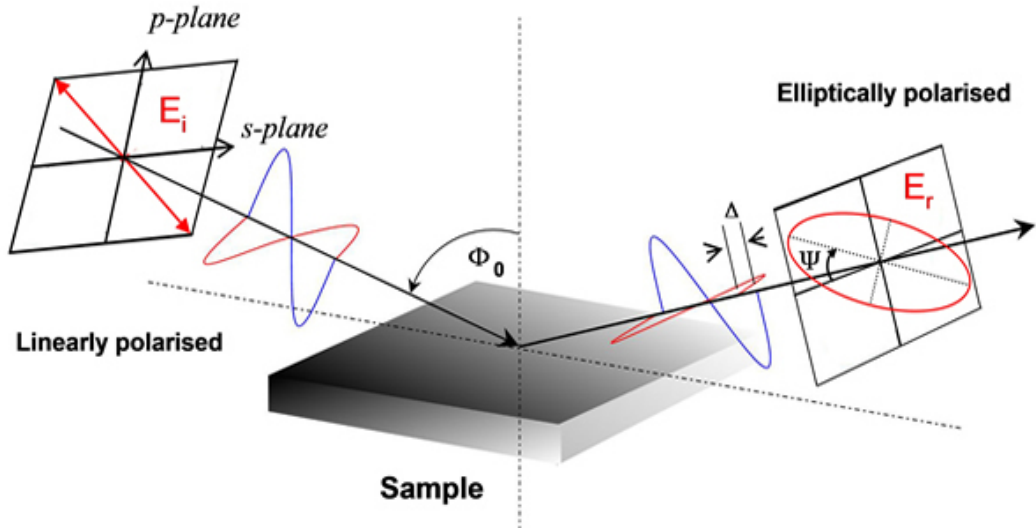


Figure 4.2: Schematic of the beam path during an ellipsometric measurement, critical parameters are indicated

350 given by $\tan \Psi$ (Ψ is the angle between the *s*-plane and the major axis of the ellipse). The last major parameter is the incident angle, denoted by Φ . A schematic diagram illustrating these parameters can be seen in figure 4.2.

From these parameters, one can directly determine the ratio between the reflectance in the *p*-plane (r_p) and the reflectance in the *s*-plane (r_s) from 355 the fundamental ellipsometric relation (eqn. 4.1). Once this relationship is known, the Fresnel equations (eqn. 4.2) can be used to numerically determine the value of the complex index of refraction at the specific wavelength of the incoming beam. The complex index of refraction (eqn. 4.3 on the following page) describes the nominal index of refraction but additionally includes an 360 imaginary term to describe absorption of light in the material (commonly referred to as the extinction coefficient, κ).

$$\rho = \frac{r_p}{r_s} = \tan(\Psi)e^{i\Delta} \quad (4.1)$$

$$r_p = \frac{\tilde{n}_1 \sqrt{1 - \left(\frac{\tilde{n}_1}{\tilde{n}_2} \sin \Phi\right)} - \tilde{n}_2 \cos \Phi}{\tilde{n}_1 \sqrt{1 - \left(\frac{\tilde{n}_1}{\tilde{n}_2} \sin \Phi\right)} + \tilde{n}_2 \cos \Phi} \quad (4.2a)$$

$$r_s = \frac{\tilde{n}_1 \cos \Phi - \tilde{n}_2 \sqrt{1 - \left(\frac{\tilde{n}_1}{\tilde{n}_2} \sin \Phi\right)}}{\tilde{n}_1 \cos \Phi + \tilde{n}_2 \sqrt{1 - \left(\frac{\tilde{n}_1}{\tilde{n}_2} \sin \Phi\right)}} \quad (4.2b)$$

$$\tilde{n} = n + i\kappa \quad (4.3)$$

This type of analysis is sufficient for thick, isotropic samples without any surface layers (e.g. surface oxides or adsorbed gases), and can directly provide the value of \tilde{n} . However, once layers are stacked upon one another, the system 365 becomes very difficult to analyze directly due to interference effects between the layers. It becomes necessary to use modeling techniques to determine the correct values of \tilde{n} and thickness (t) for each layer.

The power of ellipsometry as a high-resolution optical analysis technique stems from the use of phase and polarization changes. This allows the analysis 370 to overcome the diffraction limit, and can be accurate down to angstroms. Properly modeling the system is critical for this analysis to be as precise as possible. Thus, there have been refinements of the ellipsometric method to greatly increase the amount of experimental data points, allowing the overall system to be over-determined and thus letting all of the systems parameters 375 to be calculated.

Variable angle spectroscopic ellipsometry (VASE) is one of these variants. Spectroscopic ellipsometry differs from single-wavelength ellipsometry by utilizing a broad-band light source as opposed to a monochromatic source. By performing ellipsometric analysis at each of the wavelengths, one can determine the wavelength (and thus photon-energy) dependence of n and κ . This 380 not only helps to improve data analysis (as it can generally be safely assumed that the values of n and κ are smooth functions of λ), but allows for the determination of many other properties of the material. Of specific importance is the complex dielectric function ($\tilde{\epsilon}$), which is related to \tilde{n} by the relation shown in equation 4.4 on the next page. Knowing these functions can allow 385 for determination of electronic properties such as the bandgap energy, the absorption coefficient, amongst others. Finally, by obtaining spectra at a number

of different incident angles, one directly provides additional data points across the entire wavelength spectrum. Even a small number of additional angles can
390 quickly provide sufficient data points for the system to be over determined.

$$\tilde{\epsilon} = \epsilon_1 + i\epsilon_2 = \tilde{n}^2 \quad (4.4)$$

During this project, a VASE M-2000U system (figure 4.3) built by J.A. Woollam, inc. was used to collect all of the ellipsometric data. In addition, data analysis was performed using the WVASE32[©] package also provided by J.A. Woollam, inc. The system utilizes a rotating compensator and a CCD
395 detector to greatly decrease data collection time by collecting data across the entire spectrum simultaneously. More information on this system is available from the J.A. Woollam, inc. webpage.¹

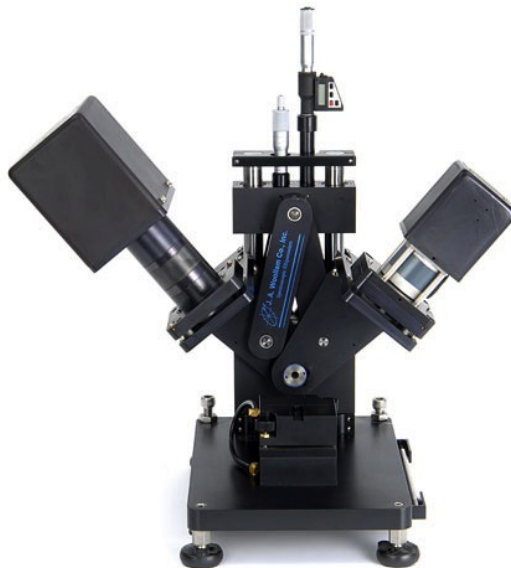


Figure 4.3: Photograph of the J.A. Woollam M-2000U variable angle spectroscopic ellipsometer (VASE)

4.3 Phase Identification

4.3.1 X-Ray Diffraction

400 Being able to identify the presence of various phases and materials was an important

X-ray diffraction (XRD) is a very commonly used technique for performing this identification. Utilizing the concepts of coherent interference, which leads

to Bragg's law of diffraction given in equation 4.5. X-rays are utilized because their wavelengths are similar to the length scales between atomic planes in crystals (1–100Å). As the incident rays pass through the sample and are reflected by atomic planes, they can either constructively or destructively interfere.

$$n\lambda = 2d \sin \theta \quad (4.5)$$

Figure 4.4 gives a graphical illustration of this principle. If the extra distance traversed by photons on the first path is equal to an integer number of wavelengths there will be constructive interference (see fig. 4.4a). However, if the θ angle is slightly changed the interference rapidly obtains destructive character (see fig. 4.4b). In this manner, if the crystal is moved through a range of $\theta - 2\theta$ values, a pattern of angles where constructive interference occurred.

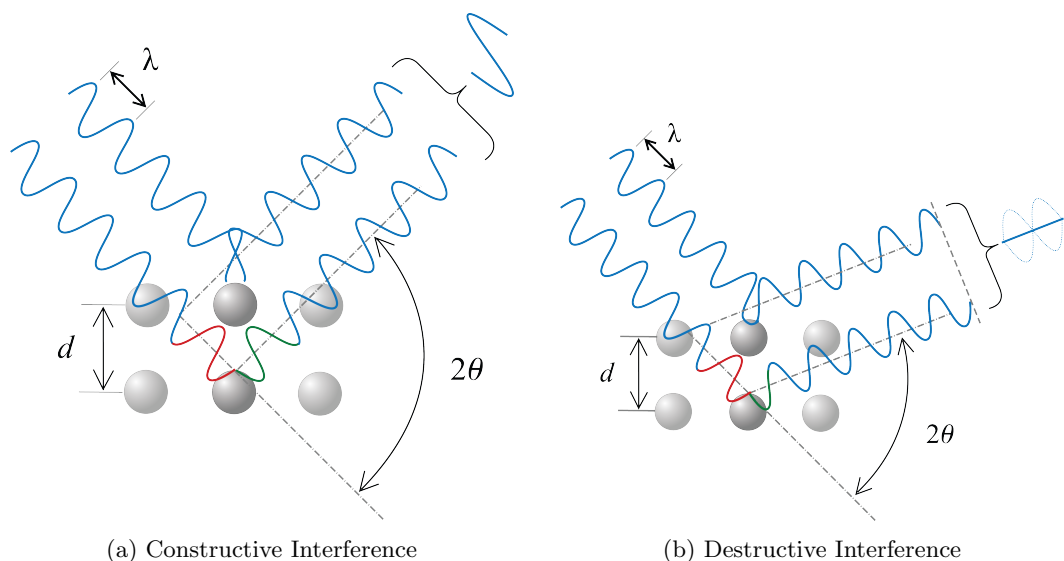


Figure 4.4: These two images illustrate the effect of interference on Bragg diffraction. In (a) the extra path length is exactly correct to allow coherence with the other ray; this causes constructive interference. (b) is the other condition, where the path length causes a phase shift of 90° and thus the rays interfere destructively.

The diffraction pattern can be used to determine a list of the interplane spacings (d-spacings) present in the sample. The values of peaks at various 2θ can be converted to d-spacings via the relation $d = \frac{\lambda}{2 \sin \theta}$. Individual materials will have a specific pattern of reflections that allow them to be identified in the sample.

This project used two XRD instruments, a Brüker D8 Discover XRD and a Rigaku SmartLab XRD (see figures 4.5 and 4.6 on page 18). Both sources

utilized a Cu-K α X-ray source ($\lambda = 1.5418\text{\AA}$). [Results from both instruments were used, but is it worth it to mention two (basically equivalent) systems]



Figure 4.5: Photograph of the Brüker D8 Discover X-ray diffractometer

4.3.2 Grazing Incidence X-Ray Diffraction

Both instruments used in this study were capable of collecting data in GIXRD mode (fixed $\omega-2\theta$).
425

4.4 Thermal Analysis

4.4.1 Thermogravimetric Analysis

Thermogravimetric analysis (TGA) is a very useful tool when attempting to determine the viability of a precursor in an ALD process. It allows for estimation of vaporization rate at various temperature rates as well as indications of chemical breakdown (i.e. thermalization) which would hinder the precursor's usefulness.
430

At its core, TGA is a measurement of mass loss as a function of temperature or time. A small sample (1–10 mg) of material is placed in a microgram balance pan and suspended inside a furnace. The furnace is then heated at a specified rate while the sample mass is carefully monitored. For the experiments used in
435

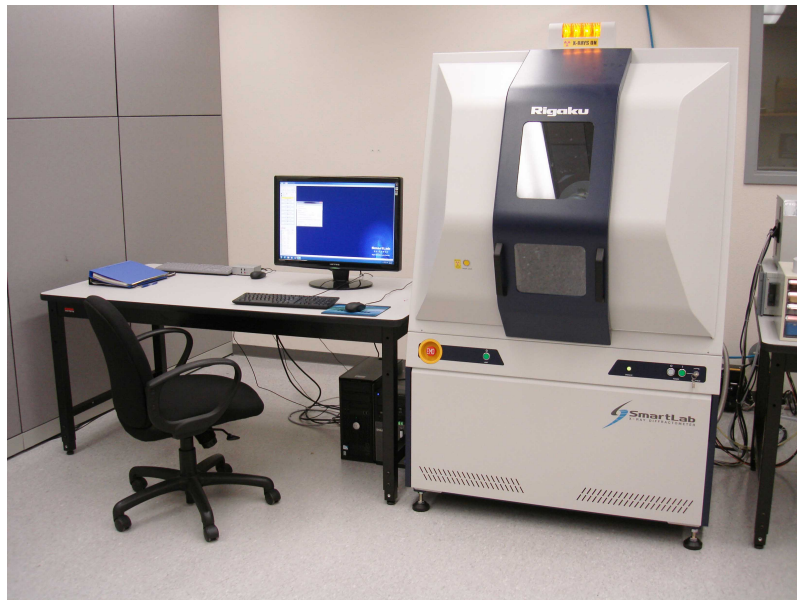


Figure 4.6: Photograph of the Rigaku SmartLab X-ray diffractometer

this study (evaluation of thermal vaporization and thermal degradation) it is important to ensure that the testing environment is inert. This is accomplished by using a platinum pan in the microgram balance and constantly purging the furnace with a small flow of dry nitrogen gas. The heating rate can be varied according to a pre-determined program to provide more information at various individual temperatures.

This technique was used to evaluate various precursor candidates for the lead oxide half of the PbTiO_3 deposition procedure. The instrument used was a Q50 TGA device (fig. 4.7a on the facing page). A detailed discussion of TGA procedures and the investigated chemicals can be found in subsequent chapters (see 7.1 on page 35).

4.4.2 Differential Scanning Calorimetry

Differential scanning calorimetry (DSC) is a technique that allows for the determination of various critical temperatures for a material, and also can highlight changes in chemical structure due to degradation or other thermal processes.

DSC is the analysis of energy absorption as a function of temperature, which is the essence of calorimetry. DSC uses a sample and reference system to isolate the energy absorbed by the sample from that of the holder pan. Sample sizes usually range from 0.1–2 mg of material; as the samples used



Figure 4.7: Photograph of the thermal analysis instrumentation used during this study, made by T.A. Instruments, inc.

in this study are volatile the sample pans are hermetically sealed to prevent mass loss. The sample and reference pans are then placed inside a thermally insulated chamber. The temperature of each is carefully monitored, and differing amounts of heat are applied to negate the temperature difference between the sample and reference. The difference in absorbed heat as a function of temperature is then given as the result. In general, experiments include both heating and cooling curves to gain a complete understanding of the different energies.

DSC was used to analyze the behavior of precursor chemicals around their evaporation and reaction temperatures. The main goal was to determine if the material underwent any thermally-activated degradation processes at either of these two temperature ranges. At the evaporation temperature, the sample was generally cycled multiple times to simulate actual use in the ALD. These measurements were taken using a Q2000 DSC system (fig. 4.7b) made by T.A. Instruments, inc.

Chapter 5

Sample Fabrication

5.1 Precursor Selection

475 5.1.1 Titanium Source

The source of titanium that was used was titanium(IV) isopropoxide ($\text{Ti}-\text{o-}i\text{-Pr}$, $\text{Ti}(\text{OCH}(\text{CH}_3)_2)_4$). This compound is very commonly used in ALD literature. [Citation needed] It is a liquid precursor with a high vapor pressure and reacts easily with most oxidizers; the most commonly used oxidant for 480 this reaction is water vapor, similar to the TMA-H₂O reaction (see section 3.3 on page 7).

5.1.2 Lead Source

Lead sources included bis(2,2,6,6-tetramethyl-3,5-heptanedionato)lead(II) (Pb(TMHD)_2) and lead(II) hexafluoroacetylacetone (Pb(HFAC)_2). Both compounds had been referenced in literature [citation needed], were available from 485 multiple chemical suppliers, and were expected to have the highest vapor pressure of the choices available at the time.

Samples of both of these compounds were obtained from Strem Chemical, inc. (sp?) Analysis of the precursors included thermal tests (TGA and DSC, 490 see section 7.1 on page 35) as well as test depositions of ALD films. The precursor chosen for use after testing was Pb(TMHD)_2 , and films discussed further solely utilized this compound.

5.1.3 Oxidizer

Three potential oxidants were considered; these included water, oxygen, 495 and an ozone/oxygen mix. The choice of oxidant depends heavily on the reactivity with the potential precursors.

The choice of titanium(IV) isopropoxide as the titanium source allows for any of the three selected oxidizers to be used. A hydrolysis reaction will occur when exposed to water vapor; in the case of oxygen or ozone the ligands will 500 be consumed via a combustion reaction.

The two lead precursors do not undergo hydrolysis when exposed to water, and as such require the use of the combustion pathway. In addition, it was found that the reaction proceeded more completely when the O₃/O₂ mixture was used. For simplicity of the process, the O₃/O₂ mix was used for both
505 half-reactions.

5.2 Substrate Preparation

Fabrication and preparation of substrates was an important part of the deposition process. Some substrates were purchased and simply cleaned, others needed to be fabricated or otherwise processed prior to cleaning and use in
510 deposition. Three main types of substrates were used: thermally oxidized single-crystalline silicon (100) wafers, silicon wafers that had a thin layer of platinum deposited on the surface, and strontium titanate (100) single crystal substrates.

5.2.1 Si(100)

515 The silicon substrates were prepared in a simple manner. 4" diameter silicon wafers with 200 nm of thermally grown oxide were diced into 1.5 cm x 1.5 cm pieces. When a sample was to be used for deposition, it was cleaned by one minute of sonication in acetone, followed by isopropanol, with a subsequent 5 minutes of sonication in deionized (DI) water. These were then air dried with
520 dry nitrogen. Finally, the substrates were cleaned in a oxygen plasma cleaning system to remove any remaining organic residues present on the surface.

5.2.2 Platinized Si(100)

Platinized silicon substrates were prepared in a similar manner to the Si(100) samples. For the initial platinization, a large piece (5 x 5 cm²) of
525 silicon wafer with a thin layer of native oxide, as opposed to the 200 nm of thermally grown oxide, was prepared in the manner described above. Then a 15 nm layer of platinum was deposited via ALD (deposition recipe can be found in redacted). The substrates were then cleaved into smaller pieces for later use.

530 If the samples are stored, it is recommended to again clean the samples in the standard procedure prior to use (see 5.2.1).

5.2.3 STO(100) and Nb:STO(100)

Oxide crystal substrates were prepared in such a fashion as to promote the formation of atomically flat terraces. This has the advantage of promoting a uniform surface species across the entire sample — the etchant used in this process leaves the sample titania-terminated.

To prepare these samples, the substrates are first pre-cleaned in a three step sonication process. The samples were cleaned for five minutes in each of acetone, methanol, and isopropyl alcohol. Subsequently, the samples were sonicated for fifteen minutes in DI water. Need to find reference and exact timings. Email Eric. The substrates were then dipped into buffered hydrofluoric acid to etch for 35 seconds, then removed and flushed with copious DI water. Once the sample is thoroughly rinsed, the samples are dried using dry nitrogen.

After the etching process, the samples are annealed at 1050°C for two hours. Once the samples are cooled, they are ready for immediate use. AFM can be used to confirm the presence of atomic terraces.

If the samples are stored, it is recommended to again clean the samples in the standard procedure (see 5.2.1 on the facing page).

5.3 Deposition Parameters

There are four main parameters that can affect the behavior of an ALD deposition. These are the growth temperature, the dosage of each precursor, the purge time between doses, and any extended precursor-surface exposure time.

5.3.1 Growth Temperature

The temperature of the growth chamber has a strong effect on reaction behavior. ALD reactions are sensitive to temperature, and will only proceed properly within a certain range known as the ‘ALD window.’ Outside of this range, the reaction enters one of a number of different regimes; these are determined by comparing the growth rate of the deposition to that of a reaction in the self-limiting saturated “ALD mode.”

If the growth temperature is less than the lower bound of the ALD window, the two regimes are condensation limited and activation energy limited. Condensation limited growth occurs when the substrate temperature is low enough that precursor condenses onto the surface without reacting with the

565 presented sites. This causes higher than expected growth rates, and a lack of self-limiting behavior. If the reaction instead proceeds into the activation energy limited regime, molecules of precursor lack sufficient energy to react with the surface. This is characterized by lower deposition rates.

570 Conversely, if the reactor temperature is excessive the reaction again become anomalous. Decomposition limited growth, characterized by excessive deposition, is a result of thermal cracking of the precursor materials. This reaction is not limited to the surface, and accounts for the extra material being deposited. Lower deposition rates indicate that the temperature is sufficient to cause desorption of previously-reacted material from the sample.

575 For an ALD run to be successful, the acceptable temperature window for all of the reactions should overlap in some temperature range. This can become difficult with reactions requiring multiple metal precursors (e.g. PbTiO_3 , a combination of TiO_2 and PbO), as these can have widely varying ALD windows for their respective reactions.

580 5.3.2 Precursor Dosage

585 The dosage of precursor or oxidant to the surface is another parameter of critical importance. An ALD reaction requires a minimal amount of precursor to sufficiently saturate the surface, while it is beneficial to minimize any excess precursor as it will be a wasted byproduct (minimizing costs, environmental impact, etc.).

The vaporization behavior of the precursor can have a dramatic impact on how simple or difficult it is to deliver a saturating dose to the surface. Some materials have readily available precursors with high vapor pressures; titanium isopropoxide and trimethylaluminum (TMA) are both liquids, and 590 tetrakis(dimethylamido)hafnium ($\text{Hf}\{\text{N}(\text{CH}_3)_2\}_4$) is a low-melting temperature solid. These are commonly used precursors for depositing their respective oxides. This vapor pressure becomes an important consideration when choosing a potential compound for use in ALD (as discussed in section 5.1 on page 21).

595 Insufficient dosing is apparent in a deposition run by a slower than average growth rate, or also as a non-uniform deposition rate across the sample. However, overdosing is not readily apparent in an ALD-mode deposition. The dose must be lowered to a point where the dose is insufficient, and then increased back to a saturating level.

600 Controlling the dose is dependent on injection time (which is the time the valve between the process line and the precursor storage vessel is open), precursor temperature, and the cycle duration (time between precursor injections). By increasing either the injection time or the precursor's temperature the dose is increased, except in some cases with low vapor pressure materials. In this
605 case, it can sometimes be found that the evaporation kinetics are slow and it takes additional time to build up a sufficient amount of vapor to provide a dose to the reactor.

If necessary, multiple doses of precursor can be delivered to the sample during each cycle to increase the total delivered dose.

610 **5.3.3 Purge Time**

Purge time is important as it gives time for the N₂ flow to flush any remaining byproducts and excess reactants from the reactor zone. It also allows time between cycles which allows for low vapor pressure precursors to regenerate evaporated material; if this time is too short to fully regenerate the dose in the
615 cylinder the precursor will eventually appear to be depleted during the course of the deposition.

5.3.4 Exposure Time

Exposure time denotes the time where the precursor is held in the reaction zone to increase the amount of time during which the surface reaction can occur. This is beneficial for two types of depositions. In the case of low-reactivity
620 precursors, it increases the amount of time that the precursor is available to the surface, greatly increasing the surface coverage per cycle. Exposure mode is also beneficial for depositing upon three dimensional structures, especially those with a high aspect ratio, e.g. nanotube templates. This extra dwell time
625 of the precursor allows for diffusion of reactant into the structure, for a uniform coverage upon the entirety of the surface. Purge time must be increased accordingly to allow for byproducts to diffuse back out of the structure.

5.4 Post-Deposition Annealing

Two types of annealing procedures were used in this study. Oven annealing,
630 with the simple use of a furnace in ambient atmosphere; and rapid thermal

annealing (RTA), characterized by very high heating and cooling rates and performed in an inert atmosphere (dry N₂).

5.4.1 Oven Annealing

In oven annealing, the samples to be processed are placed in a cold oven in the ambient atmosphere of the laboratory. The samples are then heated gradually at a rate of 10–25°C per minute up to the final annealing temperature, which ranged from 600–900°C. The samples are then allowed to heat-treat for 120 minutes at the process temperature, and then the furnace is allowed to return to room temperature.

This conventional heating pattern allows the sample to obtain its equilibrium crystalline phase composition, be that a single crystalline phase, polycrystalline, or involve multiple phases or materials. This was the annealing method most commonly used during this study.

5.4.2 Rapid Thermal Annealing

Rapid thermal annealing (RTA), as its name suggests, involves very high heating and cooling rates. RTA systems can heat at rates over 10°C per second, allowing the chamber and sample to reach the process temperature very quickly. Similarly, processing times are generally much shorter, and are generally no longer than 10–15 minutes. Cooling, facilitated by a water cooling apparatus, also occurs rapidly. These sharp gradients can have different effects on the crystal structure of the film, locking in different phases in the material that may otherwise dissociate given more time during heating or cooling.

In this study samples processed via RTA used a HeatPulse XXXX? RTA system (see fig. XX), which allowed for automatic control of the process. Sample processing conditions can be found in table A.1 on page 42 in the appendix.

Chapter 6

Data Collection and Analysis

6.1 Thermal Analysis

6.1.1 Thermogravimetric Analysis

660 6.1.2 Differential Scanning Calorimetry

6.2 VASE and Modeling

Ellipsometry was used extensively to determine a variety of properties of the material. However, the primary goal of ellipsometric analysis was to determine the film thickness, in order to be able to determine the film growth rate (in 665 terms of Å per deposition cycle) of the process.

6.2.1 Data Collection

In order to collect the experimental data, the following series of steps were followed:

1. Optics alignment
- 670 2. Ambient light compensation (DC offset)
3. Data collection at multiple angles

Alignment of the optics of the system is performed in the manner described in the manual for the ellipsometer.² The system can have focusing optics installed which diminish the spot size of the analysis, which is useful if inhomogeneity is expected in the sample as this is a major problem for analysis (two 675 of the main assumptions made by ellipsometric models are that the layers have consistent thicknesses and optical behavior across the analysis area). This is done by manually adjusting the sample stage height and the sample surface plane. The system is designed so that when the incoming signal is maximized 680 the sample is properly aligned with respect to the p- and s-planes defined by the equipment.

Once the system is aligned, the signal that is due to ambient light (not produced by the light source) must be compensated for. The M-2000U defines this as the “DC offset.”² The offset is calibrated automatically by the system
685 by blocking the light source and measuring the signal from the surroundings. As the light present in the room is generally randomly polarized, the signal will be invariant to the polarizer settings. Correctly setting this value greatly decreases the uncertainty during the analysis phase; it mainly affects the degree of light depolarization measured by the system. The ellipsometer includes
690 the depolarization in its calculation of the confidence interval for the final measurement. If the degree of ambient unpolarized light is not determined before the measurement, the depolarization will be nearly completely unrelated to the actual depolarization by the sample. In addition, the depolarization can be used by non-idealized models to determine such parameters as layer
695 thickness variation, or internal interface roughness. This process will not be used for the remainder of this discussion, but more information can be found in the manual for the M-2000U.²

After the calibration steps have been completed, data collection can be performed. Three different incident angles were used for the data collection:
700 55°, 60°, and 65°. At each angle, the data was averaged over three hundred revolutions of the compensator to minimize noise in the experimental data. The system was set up to collect depolarization data simultaneously with the ellipsometric parameters.²

If the sample is expected to be inhomogeneous, the focusing optics can be
705 used and data collected at several different locations on the sample. This can provide data on how the growth process behaves spatially, such as if there is abnormal growth near the edges of the sample but homogeneous deposition as one moves nearer to the center of the substrate.

6.2.2 Model Definition

The definition of the model is a critical part of the analysis procedure. The
710 model dictates how the software package will perform its various calculations to predict the overall optical behavior, which it iteratively compares to the experimentally determined Ψ and Δ .

Simply put, the model is defined as a bulk (semi-infinite) substrate layer,
715 with a nominal number of nano- to micrometer thick layers stacked upon it. Each layer is modeled with a prediction of optical constants at each test wave-

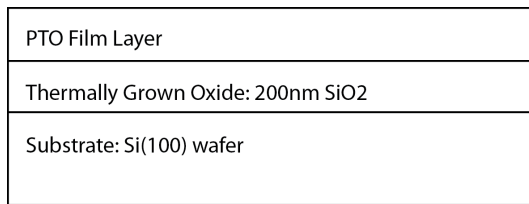


Figure 6.1: A simple graphical example of the model used for analysis of the film stack in the Si(100) samples. The parameters are t and the spectroscopic values of \tilde{n} for the PTO layer.

length. These optical constants can be provided as a table of experimentally determined results, which are available for many commonly used materials such as silicon, silica, titania, amongst others; they can also be predicted using a variety of different models. These can be empirical predictors, such as the Cauchy dispersion, or based upon physical properties of the material, oscillator-based models for example. The model types relevant to this work are discussed in more detail in subsequent sections.

The four different substrates require different material layer stacks to properly represent them, and each poses individual challenges for characterization. The Si(100) substrate that was most commonly used for this work was the simplest to model. It can be represented as a substrate layer of silicon, with a 200 nm layer of silica on top. The deposited film would be layered above the SiO_2 layer (see fig. 6.1 for a schematic representation). A large number of these substrates were analyzed for their oxide layer thickness, where the only parameter to be fit was the layer thickness. It was found that the nominal oxide layer was 200 ± 5 nm thick. This was consistent enough that 200 nm could be used for the initial thickness estimate for all samples using this substrate, and after the ALD layer was analyzed this thickness could also be included in the fit to confirm the true dimensions of the oxide layer. The substrate with thermally-grown oxide was preferred in comparison to silicon with only native oxide layer; this is because the thicker layer of transparent oxide helps to generate large oscillations in Ψ and Δ , which assists in the analysis (particularly the thickness, where the fringes are very closely related to this parameter).

6.2.3 Analysis Procedure

Once the data was collected, a specific series of steps was followed in order to obtain the highest degree of accuracy from the model. All steps were performed on the PTO layer. The modeling procedure went as follows:

- 1. High- λ Cauchy Model
- 745 2. Direct Calculation of n and κ
- 3. Conversion to Oscillator Model
- 4. Refinement of Oscillator Layer Parameters

This first step takes advantage of the transparency of the film at high wavelengths (low energies) where the photon energy is below the optical bandgap 750 of the material. In this region, the Cauchy model can be used. The Cauchy model is empirical rather than physically descriptive, and best used for amorphous materials such as polymeric films, however the assumptions required for reasonable accuracy are met when absorption in the film layer is minimized (therefore $\kappa(\lambda) \approx 0$). The equations used in the Cauchy model are shown in 755 equation 6.1. Generally, analysis during this step was performed in the spectral region where $\lambda = 600 - 1000$ nm ($E_{ph} = 2.06 - 1.24$ eV).

$$n(\lambda) = A_n + \frac{B_n}{\lambda^2} + \frac{C_n}{\lambda^4} + \dots \quad (6.1a)$$

$$\kappa(\lambda) = A_\kappa e^{B_\kappa \left(\frac{hc}{\lambda}\right) - C_\kappa} \quad (6.1b)$$

Once reasonable estimates for n , κ , and the film layer thickness are obtained at the higher wavelengths, the second step of the analysis is to generate values of \tilde{n} for the rest of the spectrum. The film thickness parameter is fixed at the 760 value determined from the Cauchy model. The values of n and κ are allowed to be determined freely without the use of a model (i.e. directly determined by use of the Fresnel relations). This type of modeling is not physical, but assists in the generation of the oscillator-based model in the next step. The software package is then instructed to run a point-by-point fit of the data from highest- 765 to lowest- λ , attempting to minimize the change in n or κ between adjacent data points.

This model is then inputted into a oscillator model. For the analysis of these films, a Tauc-Lorentz oscillator model was utilized. The oscillator models used by WVASE32 are expressed in terms of the complex dielectric function 770 $\tilde{\epsilon}$, which relates to \tilde{n} via the relationship in equation 6.2 on the next page. The Tauc-Lorentz model changes the Lorentzian model by allowing for some absorption below the fundamental bandgap energy, which would be due to defect states and other intra-band transition mechanisms. The Tauc-Lorentz

model uses the parameterization shown in equation 6.3.^{2,3} ϵ_1 is provided here
 775 in a condensed version (eq. 6.3a); the full expanded version, and its derivation
 via Kramers-Kronig integration (whose relations are shown in equation 6.4)
 from ϵ_2 , has been presented by Jellison and Modine.³

$$\tilde{\epsilon} = \epsilon_1 + i\epsilon_2 = \tilde{n}^2 \quad (6.2a)$$

$$\epsilon_1 = n^2 - \kappa^2 \quad (6.2b)$$

$$\epsilon_2 = 2n\kappa \quad (6.2c)$$

$$\epsilon_1 = \frac{2}{\pi} P \int_{E_g}^{\infty} \frac{\xi \epsilon_2(\xi)}{\xi^2 - E^2} d\xi \quad (6.3a)$$

$$\left\{ \begin{array}{ll} \epsilon_2(E) = \frac{AE_0C(E - E_g)^2}{(E^2 - E_0^2)^2 + C^2E^2} \cdot \frac{1}{E} & E > E_g \\ \epsilon_2(E) = 0 & E \leq E_g \end{array} \right. \quad (6.3b)$$

$$(6.3c)$$

$$\epsilon_1(\omega) - 1 = \frac{2}{\pi} P \int_0^{\infty} \frac{\omega' \epsilon_2(\omega')}{\omega'^2 - \omega^2} d\omega' \quad (6.4a)$$

$$\epsilon_2(\omega) = -\frac{2\omega}{\pi} P \int_0^{\infty} \frac{\epsilon_1(\omega') - 1}{\omega'^2 - \omega^2} d\omega' \quad (6.4b)$$

780 The WVASE32 software package allows one to use a graphical interface to
 provide initial guesses for the various fit parameters. At times this required
 multiple oscillators to best fit the predicted ϵ_2 function. Once this has been
 set, all of the parameters affecting ϵ_2 (A, E_0, C, E_g) are marked to be included
 in the fit. The software is then instructed to perform a best-fit of the oscillator
 785 to ϵ_2 . Once this operation completes, the software is set to fit to ϵ_1 and only
 the value of the ϵ_1 offset is allowed to be fit. Finally, the software is set to
 optimize vs both ϵ_1 and ϵ_2 , and all parameters are included. This completes
 the initial setup of the oscillator model.

Finally, the model is set to also allow the layer thickness to be fit and a
 790 general fit to the entire experimental dataset is performed. This provides the
 best guess to the physical values of the film. The thickness calculated by this
 procedure matches very closely to measurements performed by other methods
 (e.g. SEM imaging or AFM measurement of a lithographically created step).

If similar deposition parameters are utilized, it is possible to save the parameterized model for later use.⁷⁹⁵ This allows the analysis to be streamlined when the material is expected to remain constant, for example if tests of deposition at different layer thicknesses are performed. In this case, the material would have optical behavior very similar to the initial sample, and the oscillator model would be sufficiently close to valid parameters to be used directly for fits.⁸⁰⁰ All that would need to be adjusted initially would be the estimated layer thickness. If the fit fails to produce useful data, such as unreasonable values for any of the parameters or very large confidence intervals, it is recommended to proceed with the entire standard analysis procedure.

Further analysis can be performed to estimate the bandgap of the layer,⁸⁰⁵ via Tauc plot analysis. The method requires the calculation of the absorption coefficient (α) from the value of k for the layer (see equation 6.5). α is usually provided in terms of cm^{-1} , so if the wavelength is provided in nanometers a corresponding factor of 10^7 must be incorporated as well. Subsequently, a Tauc plot is constructed using a combination of α and the photon energy.⁸¹⁰ For direct bandgap materials the Tauc parameter is given by $(\alpha E_{ph})^2$. If the bandgap is of the indirect type, the function is changed to $\sqrt{\alpha E_{ph}}$. The bandgap parameter matches well to literature values (when using standard samples of well defined materials, such as a thin layer of titania). It must be noted that the bandgap that is calculated is the overall bandgap of the layer,⁸¹⁵ which may be a combination of multiple phases or materials.

$$\alpha = \frac{4\pi k}{\lambda} \quad (6.5)$$

Experimental data sets, the resulting fitted models, and Tauc analyses for selected samples are presented in appendix A.7 on page 52.

6.3 Composition Analysis

In order for the desired phase to be preferred, without any impurity phases⁸²⁰ precipitating, it is important to be able to control the stoichiometry of the produced film. Previous reports have shown that there is a close relationship between the composition of the film and the final resultant phase (see figure 6.2 on the next page).⁴

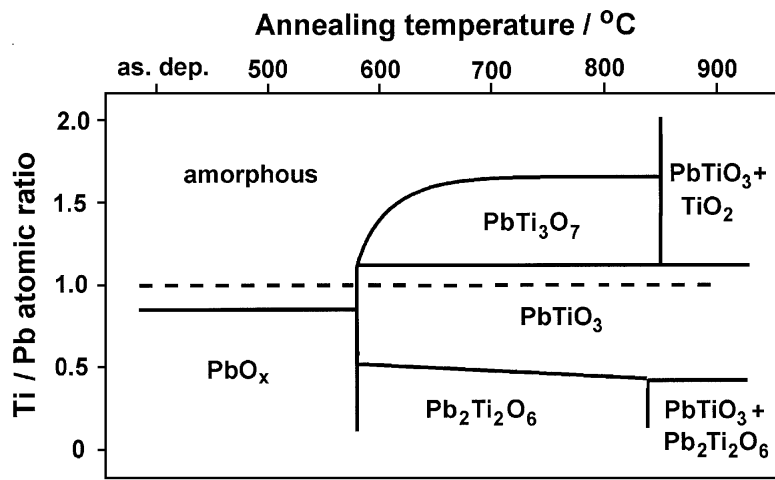


Figure 6.2: Graphic illustrating preferred phase of an annealed film at a range of stoichiometric ratios and annealing temperatures. A slight excess of Pb in the system is expected to help stabilize the perovskite PbTiO_3 phase.⁴

6.3.1 X-Ray Fluorescence Spectroscopy

825 X-ray Fluorescence was the primary method for determining the composition of the deposited films. Analysis is performed much

Initial calibration of the system is critically important to acquiring accurate measurements. Calibration is performed using a pair of standard samples of known composition, which include all elements that are to be quantified. For 830 this study, a pellet of commercially prepared PbTiO_3 powder and a thin film of $\text{PbZr}_{0.52}\text{Ti}_{0.48}\text{O}_3$ were used as standards.

6.4 X-Ray Diffraction

6.4.1 Grazing Incidence XRD

For each sample, the value of ω was set to be 80% of the film's critical angle 835 which was determined prior to the scan.

Chapter 7

Results

As discussed, the goal of this study was to determine methods for atomic layer deposition of ferroelectric oxides. In the process of realizing this goal
840 there were a number of different areas of study. The first is the analysis of thermal and chemical behavior of the various potential precursors, during which TGA and DSC were primarily used (see [6.1 on page 27](#)). Secondly, the analysis of the film growth behavior under various conditions, this was primarily measured and analyzed using the ellipsometric techniques discussed
845 earlier (see [6.2 on page 27](#)). Third, the film deposition needed to be tuned to produce films with a stoichiometric composition, as this was expected to produce films which would crystallize into the desired perovskite phase, see section [6.3 on page 32](#) for the methods used for this characterization. Fourth, the phase of the crystallized film was analyzed in detail to determine behavior
850 of the films post-annealing. XRD was used extensively for this task (see [6.4 on page 33](#)).

7.1 Thermal Analysis

While a viable titanium precursor was well identified in literature as well as experimentally, as was the oxidizers that were used, there was no such universally accepted chemical used in ALD to provide a source of lead. The primary issue was either a lack of chemical stability or a undesirably low volatility in
855 the compounds that currently were being used. TGA and DSC was performed on a number of potential candidates (see [5.1 on page 21](#) for more details) in order to gauge the performance of these materials.

860 7.1.1 Thermogravimetric Analysis

Thermogravimetric analysis allows for the estimation and comparison of volatility between multiple samples. It was used in this study to compare $\text{Pb}(\text{HF}\text{Ac})_2$ and $\text{Pb}(\text{TMHD})_2$, primarily their individual volatilities — by analyzing the mass loss at various temperatures — and whether or not there are

865 indications of imperfect evaporation. The data collected for these materials can be found in section A.5.1 on page 45.

By analyzing the TGA curve for $\text{Pb}(\text{HFAc})_2$, found in figure A.2a on page 45, there are a number of features that are immediately noticeable. First of these is the multiple stages of evaporation present in the curve. These occur 870 at approximately 170, 190, and 230°C. A TGA curve for a material that is purely evaporative, e.g. pure water, will have a single step in the curve. Additional steps indicate that other processes are activating, and causing changes to the compound affecting the mass loss.

More detail can be seen by performing a derivation on the TGA curve, giving 875 the mass loss rate. This plot can be found in figure A.2b on page 45. This plot shows a shoulder on the primary evaporative peak, and then another peak starting at around 170°C and peaking at 190°C. The shoulder indicates that even during the evaporation of most of the material, a secondary mechanism is activating causing additional mass loss.

880 **7.1.2 Differential Scanning Calorimetry**

7.2 Ellipsometry

7.3 Composition

Be sure to note the issues with composition measurements of PTO on STO. Surface limited/depth sensitive measurements required but not readily 885 available.

7.4 X-Ray Diffraction

Chapter 8

Conclusions

8.1 Future Work

890 While the work presented herein is noteworthy, and lays a framework for further investigation and refinement of ALD deposited perovskite oxides including the topic of discussion of this thesis, there is much left to be investigated in this line of research. Next steps would serve to further refine the process to improve the reliability of deposition, improving the phase purity
895 and improve the degree of epitaxy of the grown film, or better conserve and deliver precursor (issues that plagued this project throughout its course). Being able to consistently produce films of constant quality would make this work applicable to a myriad of systems.

900 Additionally, there is one aspect of film characterization that had not been investigated thoroughly during the course of this project: the ferroelectric character of the films. Verification of ferroelectric behavior, even initially in isolated grains, would greatly improve the value of the method. Initial tests would likely require the use of microscopy techniques, e.g. piezoelectric force microscopy (PFM); more standard ferroelectric measurements could likely be
905 utilized with improved film quality.

Following this path of discussion quickly leads to the question of doping the films in order to improve properties. As an example, it is well known [citation needed] that a solid solution of PbTiO_3 and PbZrO_3 greatly improves polarizability as well as the energy required to switch the film (???).

910 Finally, it would be useful to extend this method to completely novel material systems. BaSrTiO_3 is another commonly used ferroelectric material (and valuable due to its lack of lead content), and BiFeO_3 is another interesting perovskite as it presents multiferroic behavior as opposed to simply ferroelectricity.

₉₁₅

Bibliography

- [1] J. A. Woollam Co., Inc. M-2000 ellipsometer. http://www.jawoollam.com/m2000_home.html.
- [2] J. A. Woollam Co., Inc. *Guide to Using WVASE32*, 2009.
- [3] Jr. G. E. Jellison and F. A. Modine. Parameterization of the optical functions of amorphous materials in the interband region. *Applied Physics Letters*, 69(3):371–373, 1996.
- [4] J Harjuoja, A Kosola, M Putkonen, and L Niinisto. Atomic layer deposition and post-deposition annealing of PbTiO thin films. *Thin Solid Films*, 496(2):346–352, February 2006.
- ₉₂₅ [5] iXRF Systems, Inc. fx-sem xrf system. <http://www.ixrfsystems.com/products/xrf/bulk-xrf>.
- [6] Cambridge NanoTech, inc. Savannah s100 series ald. <http://www.cambridgenanotech.com/products/savannah.php>.

Appendix A

⁹³⁰ Supplemental Information

A.1 List of Chemicals

	Ph ₄ Pb
	Ti—o—i—Pr
	Pb(TMHD) ₂
935	Pb(HFAc) ₂
	Buffered HF
	N ₂
	O ₂
	O ₃
940	H ₂ O
	IPA
	Acetone

A.2 List of Samples

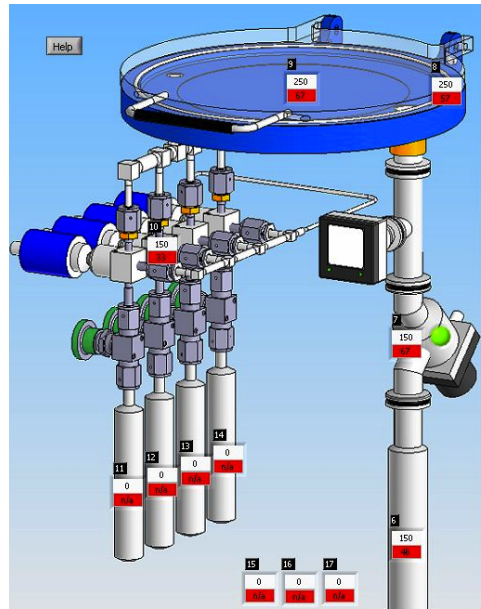
Table A.1: A list of samples used during the course of this project.

Temp. (°C)	Run #	Pb:Ti Ratio	Cycles	Subs. Type	Annealing			XRD
					Type	Temp. (°C)	Time (min)	
200	3	1:1	250	Si	None	N/A	N/A	No
	2	1:2	250	Si	None	N/A	N/A	No
	30	3:1	160	Si	None	N/A	N/A	No
				Pt-Si	None	N/A	N/A	No
250	0	1:1	625	Si	Oven	650	120	Yes
					Oven	900	120	Yes
					RTA	900	10	No
	1	1:1	475	Si	None	N/A	N/A	No
	6	1:2	250	Si	None	N/A	N/A	No
	13	3:1	250	Si	None	N/A	N/A	No
	16	3:1	150	Si	RTA	650	1	No
	19	3:1	100	Si	None	N/A	N/A	No
				Pt-Si	None	N/A	N/A	No
	20	3:1	200	Si	None	N/A	N/A	No
				Pt-Si	Oven	650	90	Yes
	21	3:1	150	Si	None	N/A	N/A	No
				Pt-Si	Oven	650	90	No
22	3:1	150	Si	None	N/A	N/A	N/A	No
			Pt-Si	Oven	650	90	Yes	
	23	3:1	200	Si	None	N/A	N/A	No
			Pt-Si	Oven	650	90	Yes	
28	3:1	120	STO	Oven	650	90	Yes	

A.3 ALD Reactor Diagram



(a) Photograph



(b) Schematic Diagram

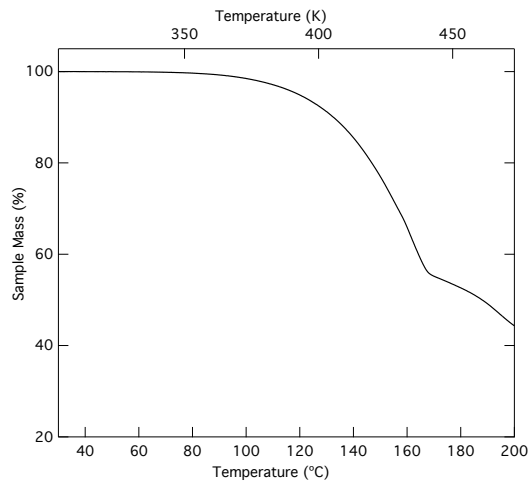
Figure A.1: Cambridge NanoTech, inc. Savannah S100 ALD reactor. Precursors are stored in heated cylinders, flow up to the reaction zone, and byproducts are pumped out of the vacuum line on the right side. Each zone can be individually temperature controlled.

A.4 Recipes for S100 ALD System

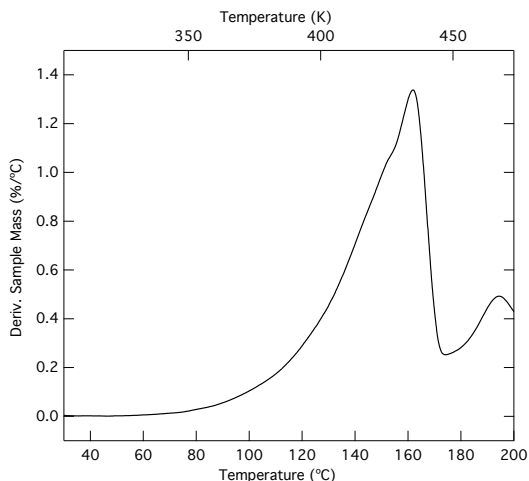
Should recipes be provided? They'd be rather specific to the instrumentation, and some of the recipes are provided by CNT (able to freely publish them?). This section would be trivial to construct, or remove entirely.

A.5 Thermal Analysis Results

950 A.5.1 Thermogravimetric Analysis



(a) Mass vs. Temperature



(b) Derivative of Mass vs. Temperature

Figure A.2: Plots of the results from TGA experiments on $Pb(HF\text{Ac})_2$. The plot shown in (a) gives the raw data showing the current mass as a function of temperature. (b) gives the same data, transformed to show the derivative of mass. Thus (b) shows the rate of mass loss at a given temperature. Initial sample mass: 6.092 mg

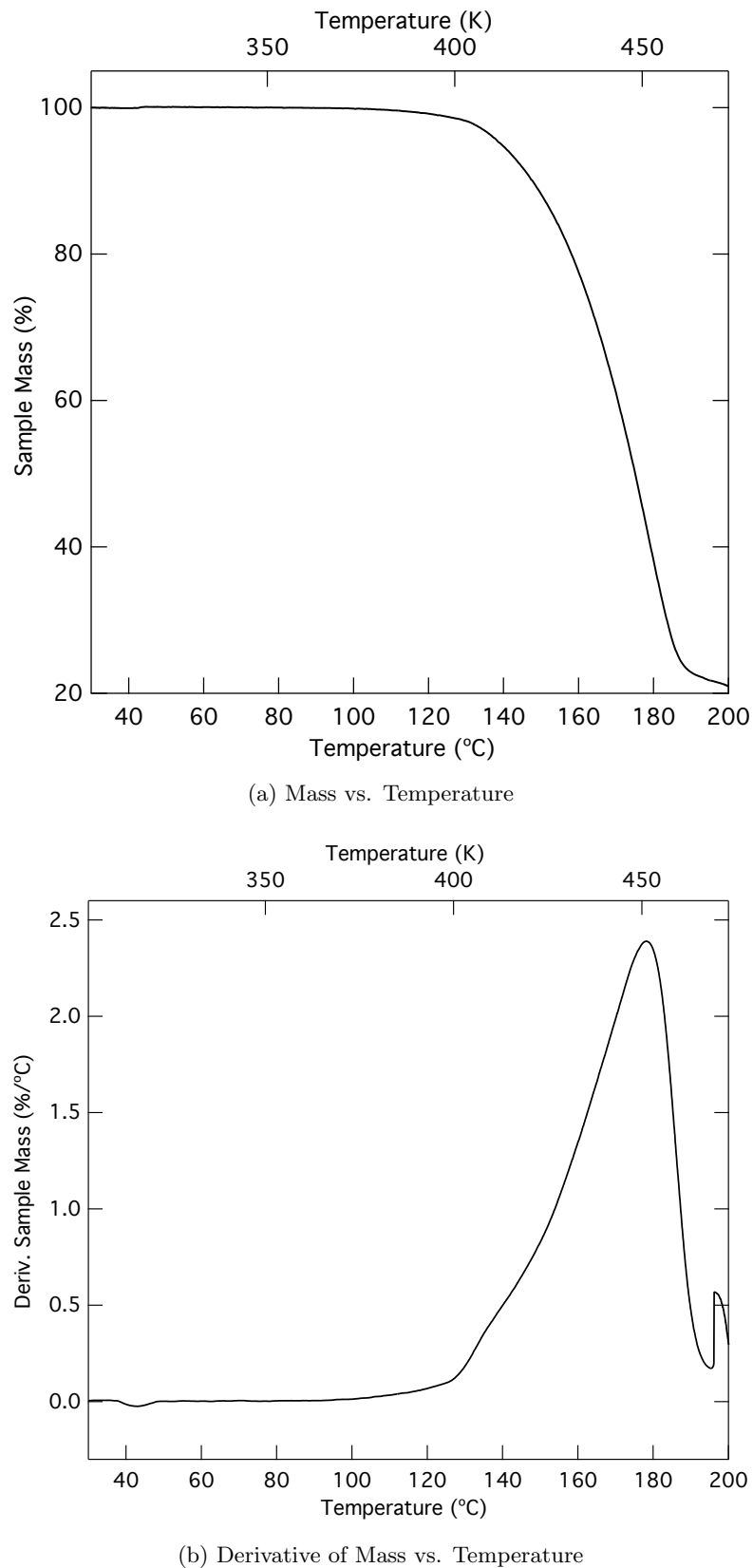


Figure A.3: Plots of the results from TGA experiments on $\text{Pb}(\text{TMHD})_2$. As in figure A.2 on the previous page, (a) presents the actual mass as a function of temperature, while (b) gives the derivative of that function. Initial sample mass: 3.719 mg

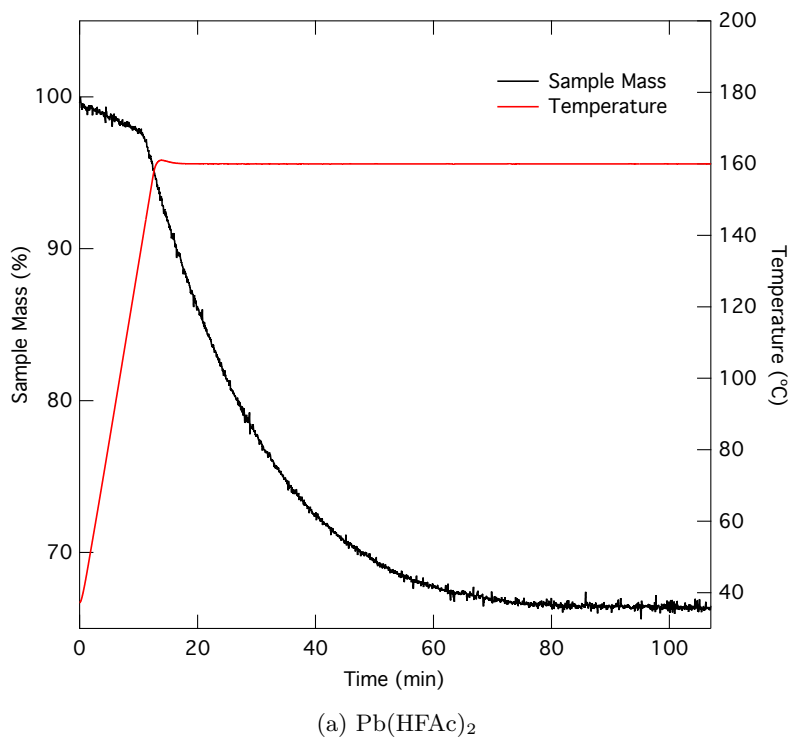
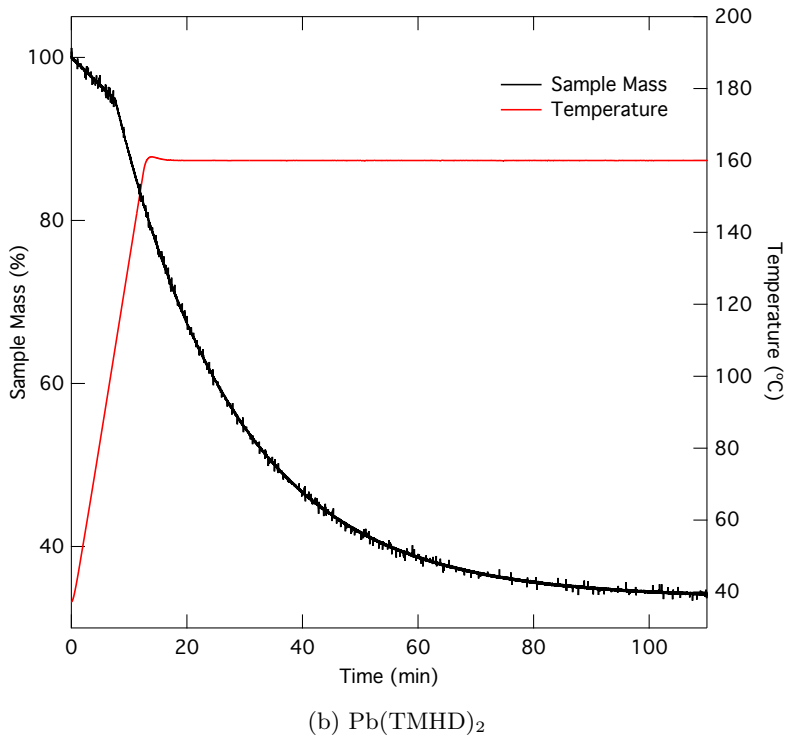
(a) $\text{Pb}(\text{HFAc})_2$ (b) $\text{Pb}(\text{TMHD})_2$

Figure A.4: Plots of the results from ramp-and-hold TGA experiments designed to investigate residual material after complete evaporation at a given temperature. From the TGA experiments seen above (figs. A.2 on page 45 and A.3 on the preceding page), a common temperature of 160 $^{\circ}\text{C}$ was chosen for this experiment. Sample sizes were 3.921 mg and 4.381 mg for $\text{Pb}(\text{HFAc})_2$ and $\text{Pb}(\text{TMHD})_2$ respectively.

A.5.2 Differential Scanning Calorimetry

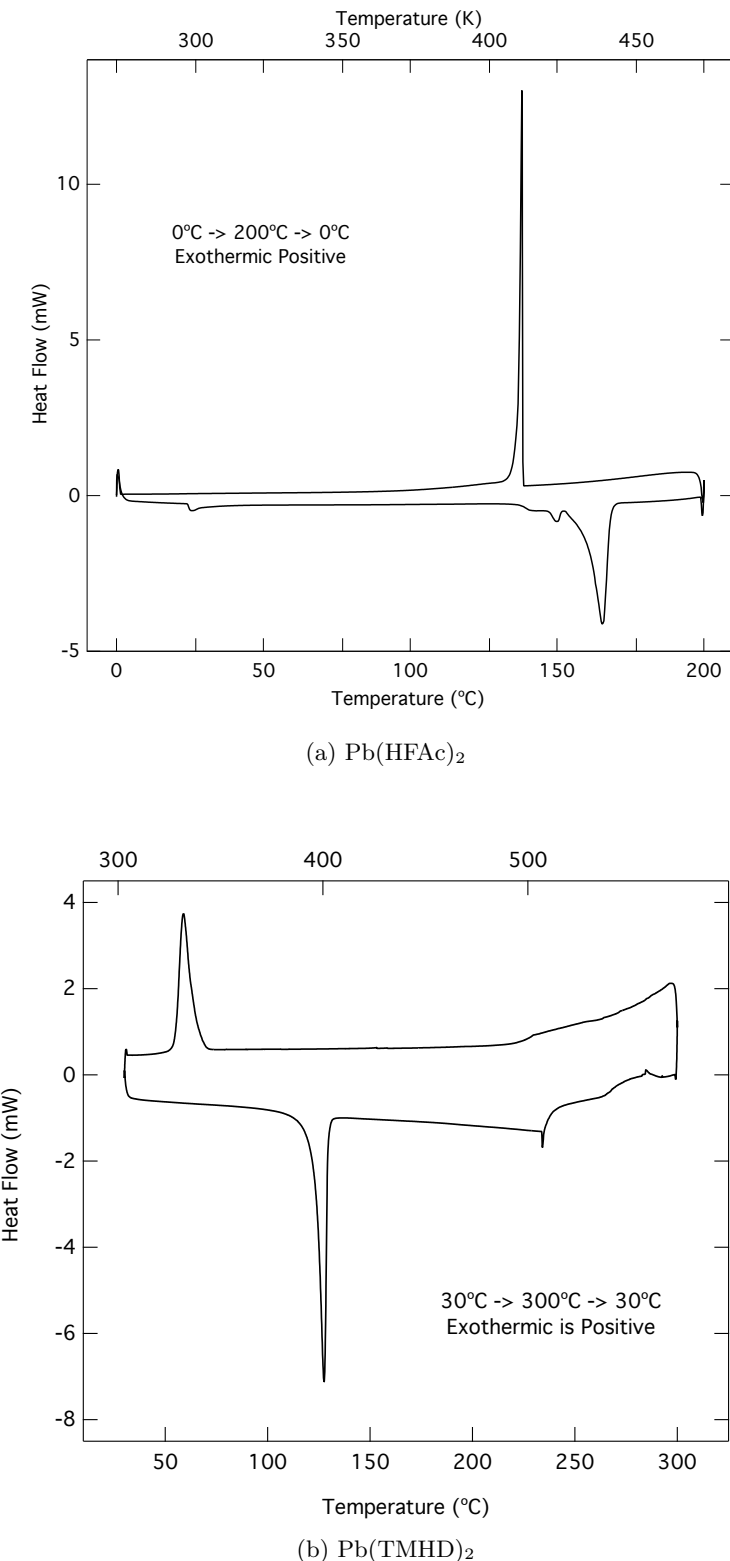


Figure A.5: This plot shows results from DSC experiments carried out during the course of this project. (a) shows the results from analyzing the $\text{Pb}(\text{HFAC})_2$ compound. (b) gives the data from $\text{Pb}(\text{TMHD})_2$. Exothermic (heat release) flow is positive in both plots.

A.6 Composition Results

Table A.2: Calculated compositions of selected samples, determined via XRF.

Run #	Substrate	Composition (%)		
		Lead	Titanium	Ti:Pb Ratio
0	SiO ₂	55.99	44.01	0.786
1	SiO ₂	55.00	45.00	0.809
13	SiO ₂	53.96	46.04	0.853
16	SiO ₂	49.45	50.55	1.022
19	SiO ₂	65.87	34.13	0.518
	Pt-Si	42.86	57.14	1.333
20	SiO ₂	56.52	43.48	0.769
	Pt-Si	51.43	48.57	0.944
21	SiO ₂	69.60	30.40	0.437
	Pt-Si	56.08	43.92	0.783
22	SiO ₂	67.64	32.36	0.478
	Pt-Si	56.06	43.94	0.784
23	SiO ₂	66.89	33.11	0.495
	Pt-Si	49.06	50.94	1.038
24	SiO ₂	68.96	31.06	0.450
	Pt-Si	62.16	37.84	0.609

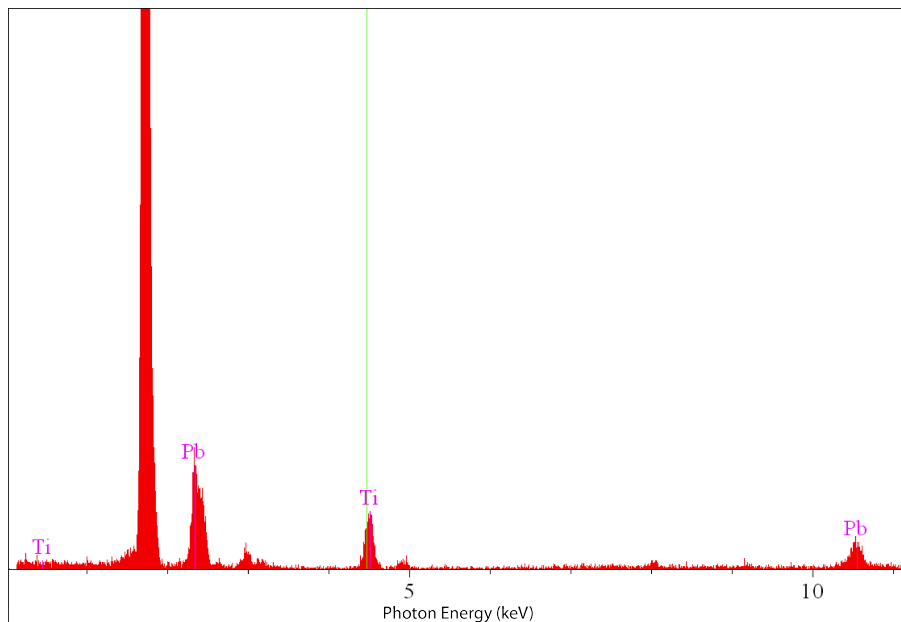


Figure A.6: The XRF spectrum collected from deposition run #0.

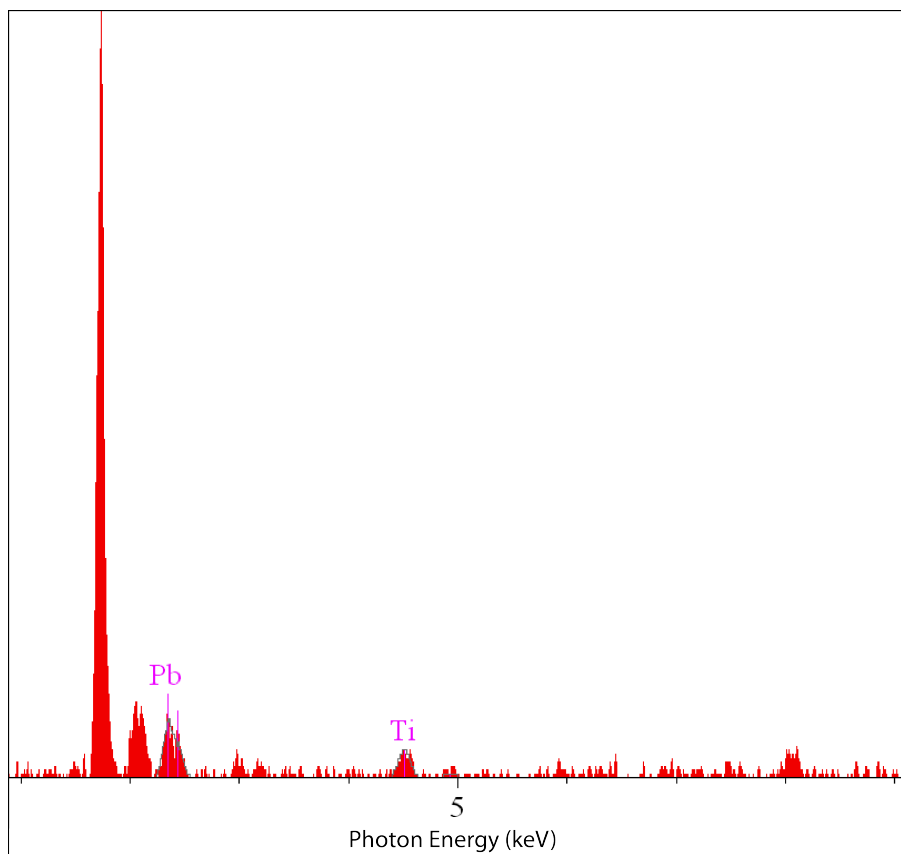


Figure A.7: The XRF spectrum collected from deposition run #20 deposited on platinized silicon. The peak between the substrate and Pb is that of Pt.

A.7 Ellipsometry Results

Table A.3: Variables used to produce the model fit for PTO #0 seen in fig. A.8 on the next page.

Layer	Variable	Thickness (nm)	Value
2. T-L Osc.		81.56	
	ϵ_1 offset		2.491
	Amp		12.662
	E_n		4.604
	C		1.351
	E_g		0.856
1. SiO ₂		203.69	
0. Si		Substrate	

Table A.4: Variables used to produce the model fit for PTO #20 seen in fig. A.10 on page 55.

Layer	Variable	Thickness (nm)	Value
3. T-L Osc.		88.77	
	ϵ_1 offset		3.619
	Amp		36.542
	E_n		4.505
	C		1.298
	E_g		2.071
2. Pt		15.052	
1. SiO ₂		1.103	
0. Si		Substrate	

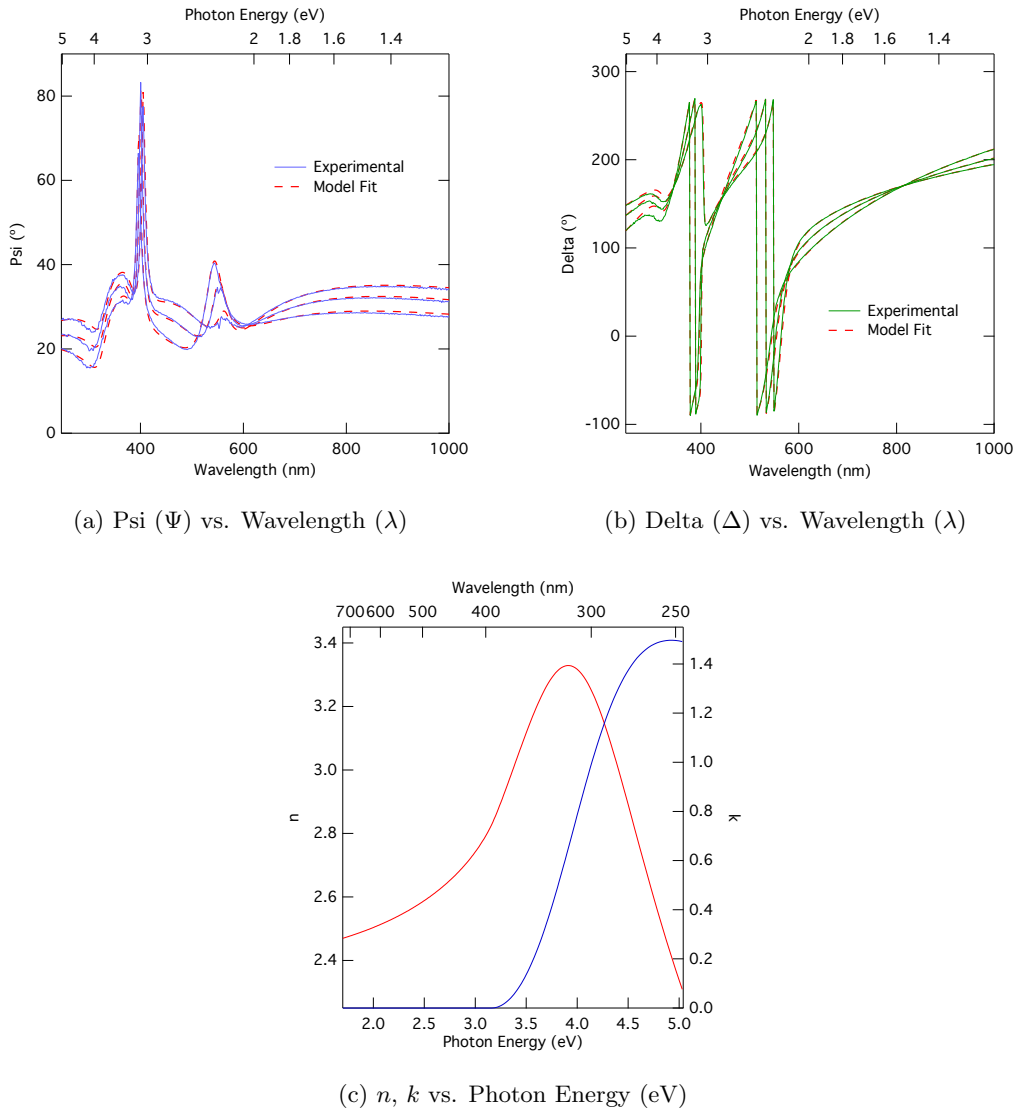


Figure A.8: The set of plots shown above show the results from ellipsometric analysis on sample #0 (see table A.1 on page 42) grown on a silicon wafer and subsequently annealed. (a) and (b) show the data and the modeled fit from the experiment. (c) shows the components of the complex index of refraction (\tilde{n}), n and k . Band gap estimation was performed using the values of k . The highlighted portion of k is the nearly linear region used in this analysis.

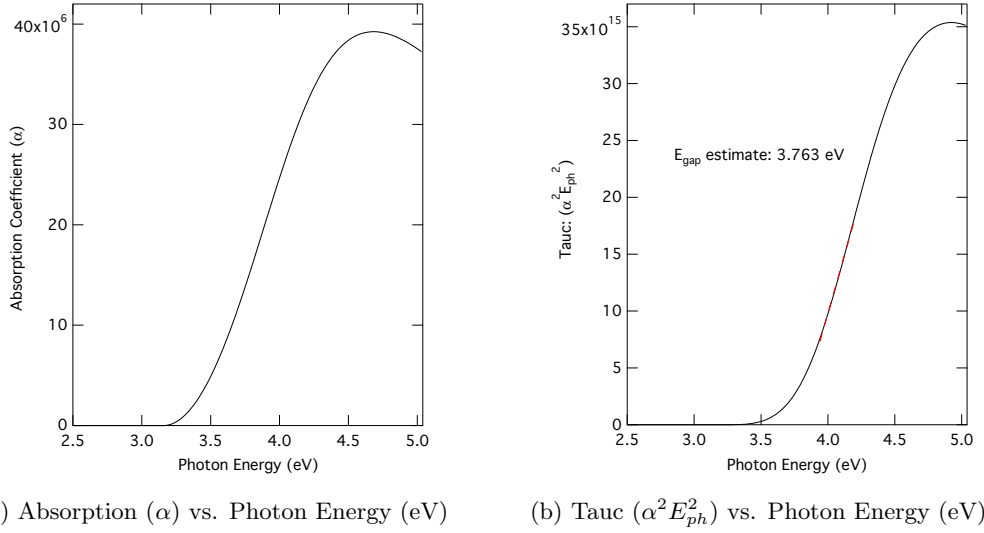


Figure A.9: Tauc analysis used to determine the bandgap of PTO #0. (a) shows the values of the absorption coefficient (α) calculated from k (seen in figure A.8c on the previous page). (b) shows the Tauc plot, the linear region can provide an estimate of the bandgap of the material.

Table A.5: Variables used to produce the model fit for PTO #28 seen in fig. A.12 on page 57.

Layer	Variable	Thickness (nm)	Value
1. T-L Osc. (2)		88.77	
	ϵ_1 offset		1.419
	Amp ₁		64.706
	E _{n1}		3.692
	C ₁		4.441
	E _{g1}		1.549
	Amp ₂		1.547
	E _{n2}		2.120
	C ₂		0.757
	E _{g2}		0.001
0. STO	Substrate		

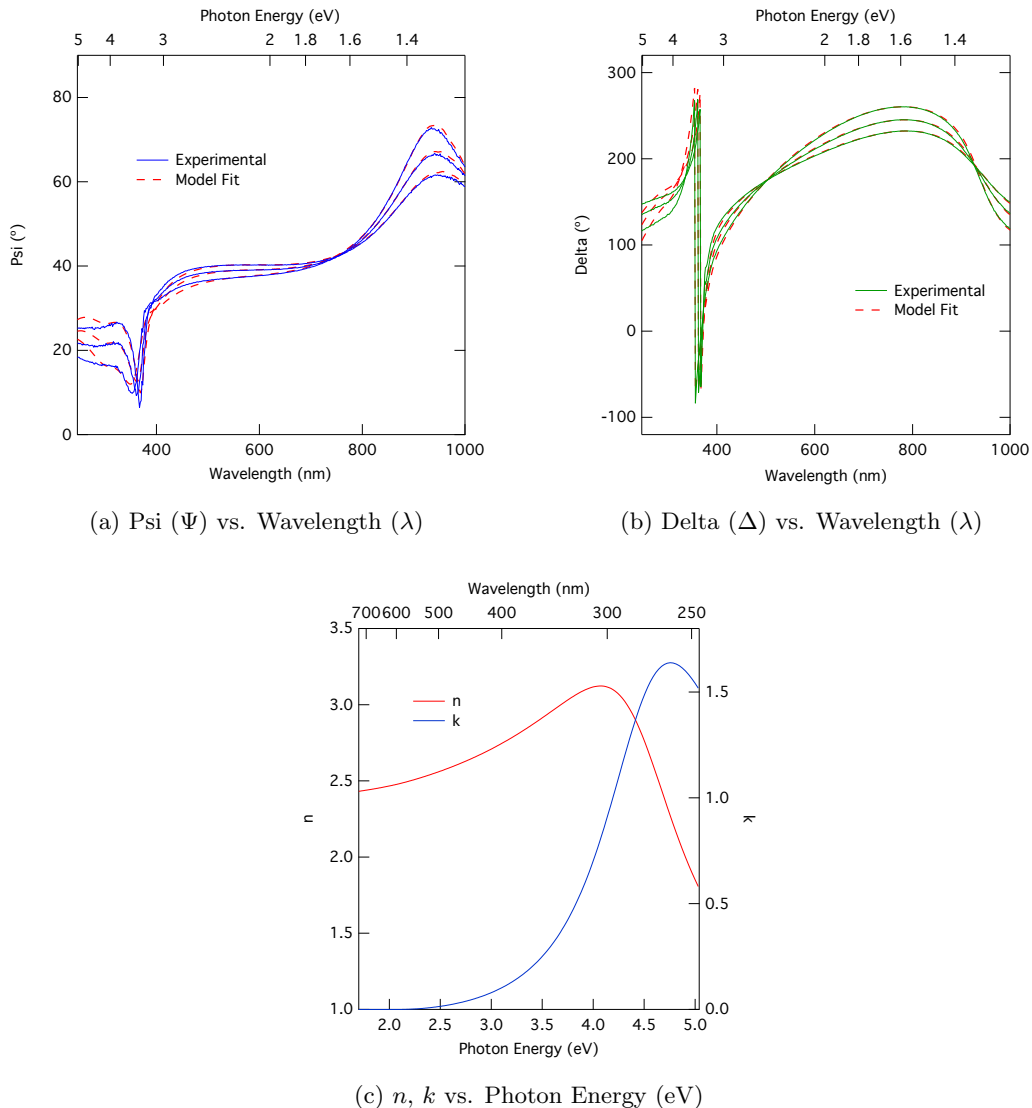


Figure A.10: Results of ellipsometric analysis on sample #20, deposited on a platinized silicon substrate. As in fig.A.8, (a) and (b) show the experimental data and model fits of psi and delta (respectively). (c) gives the plot of calculated n and k . For model parameters, see table A.4 on page 52

Table A.6: Band gap energies, determined via Tauc analysis of ellipsometric data

Run #	Subs.	Type	Band Gap (eV)
0	Si		3.763
20	Pt-Si		4.058
28	STO		3.506

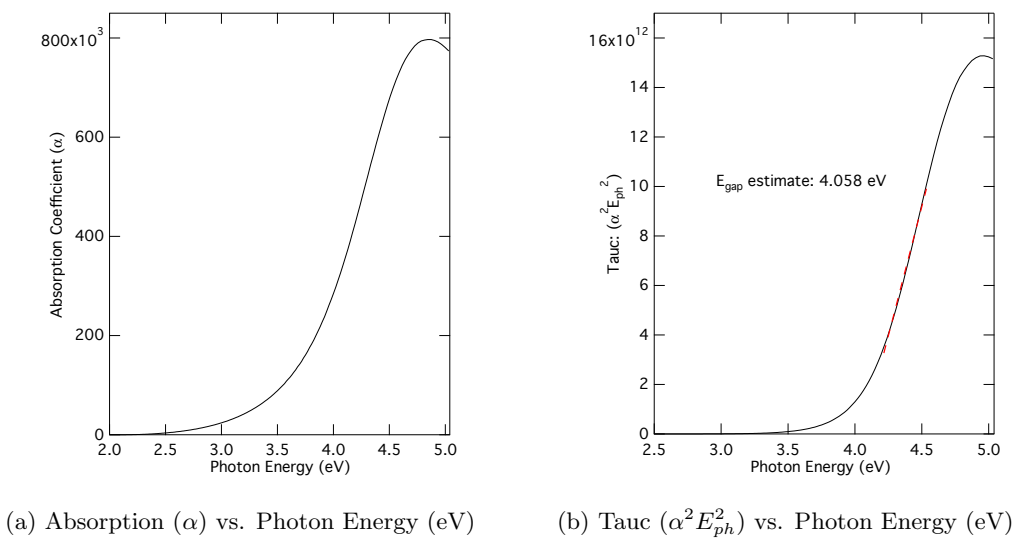


Figure A.11: Tauc analysis of sample #20 on Pt-Si

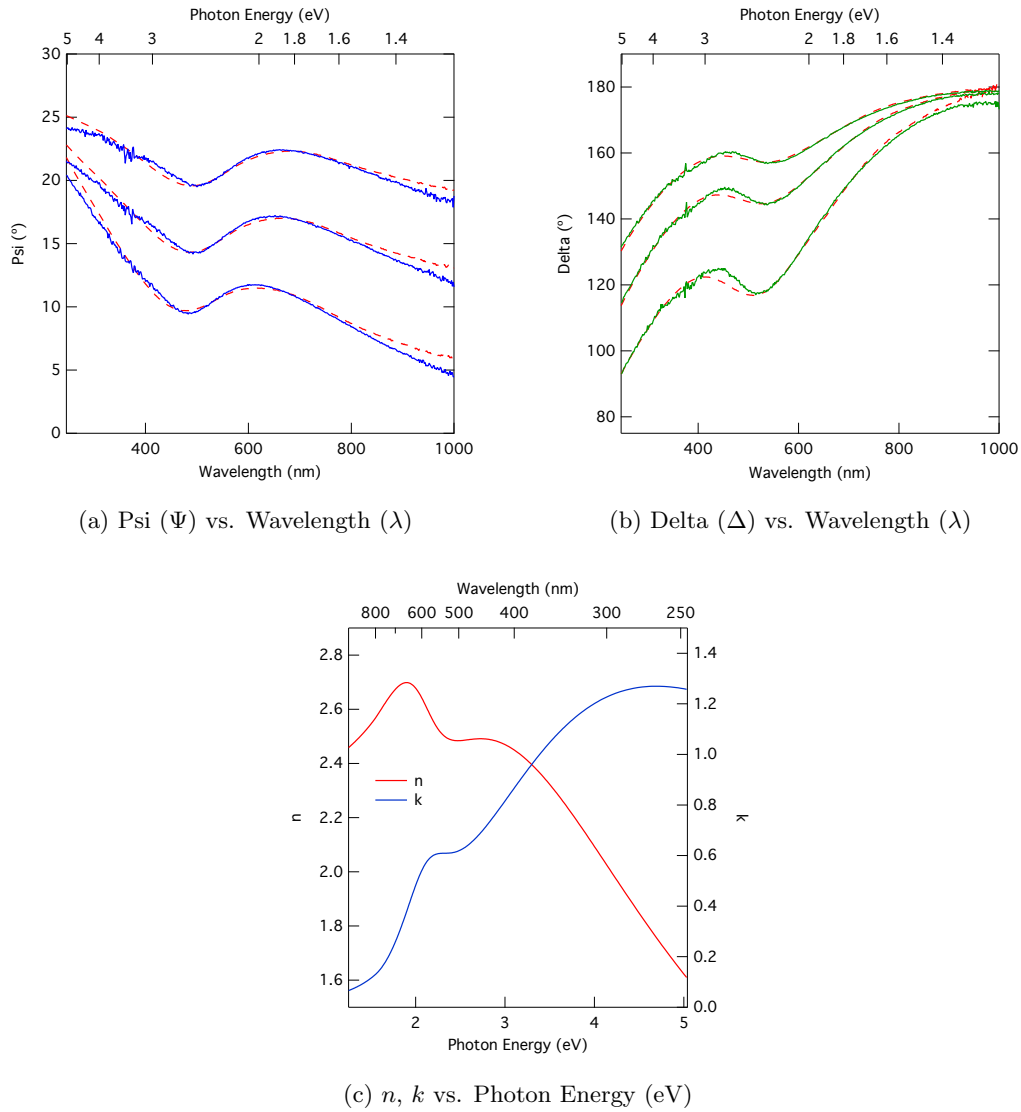
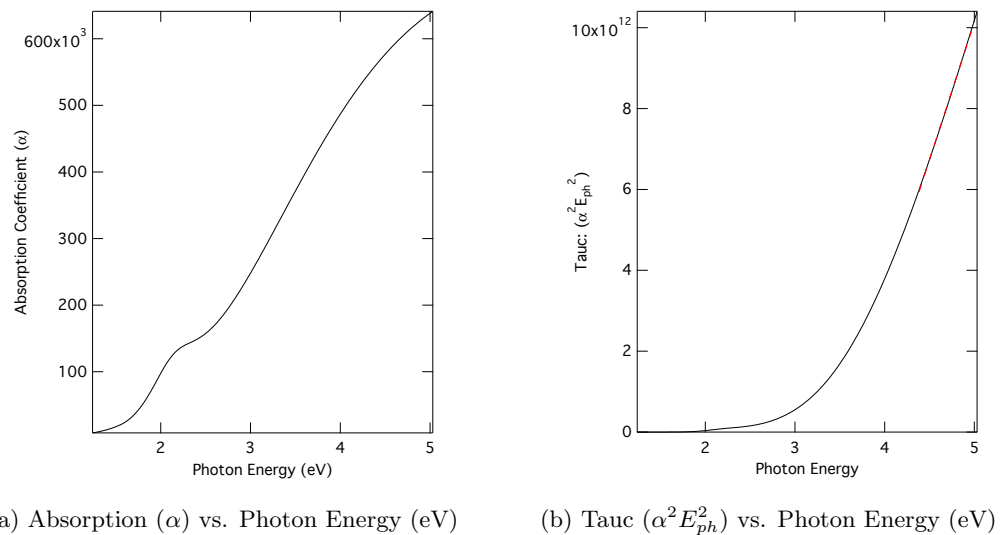


Figure A.12: Results of ellipsometric analysis on sample #28, deposited on a strontium titanate $SrTiO_3(100)$ single crystalline substrate. As in fig. A.8, (a) and (b) show the experimental data and model fits of psi and delta (respectively). (c) gives the plot of calculated n and k . This sample would not model well without a second oscillator, which gives rise to the secondary peaks in the n , k , and α plots (see fig. A.13a on the following page). For model parameters, see table A.5 on page 54.



(a) Absorption (α) vs. Photon Energy (eV) (b) Tauc ($\alpha^2 E_{ph}^2$) vs. Photon Energy (eV)

Figure A.13: $E_g = 3.506$. Tauc analysis of sample #28 - STO. Notice that the second oscillator can be seen in the absorption coefficient (a), but does not affect the shape of the Tauc plot (b) and thus does not interfere with bandgap estimation.

A.8 XRD Results

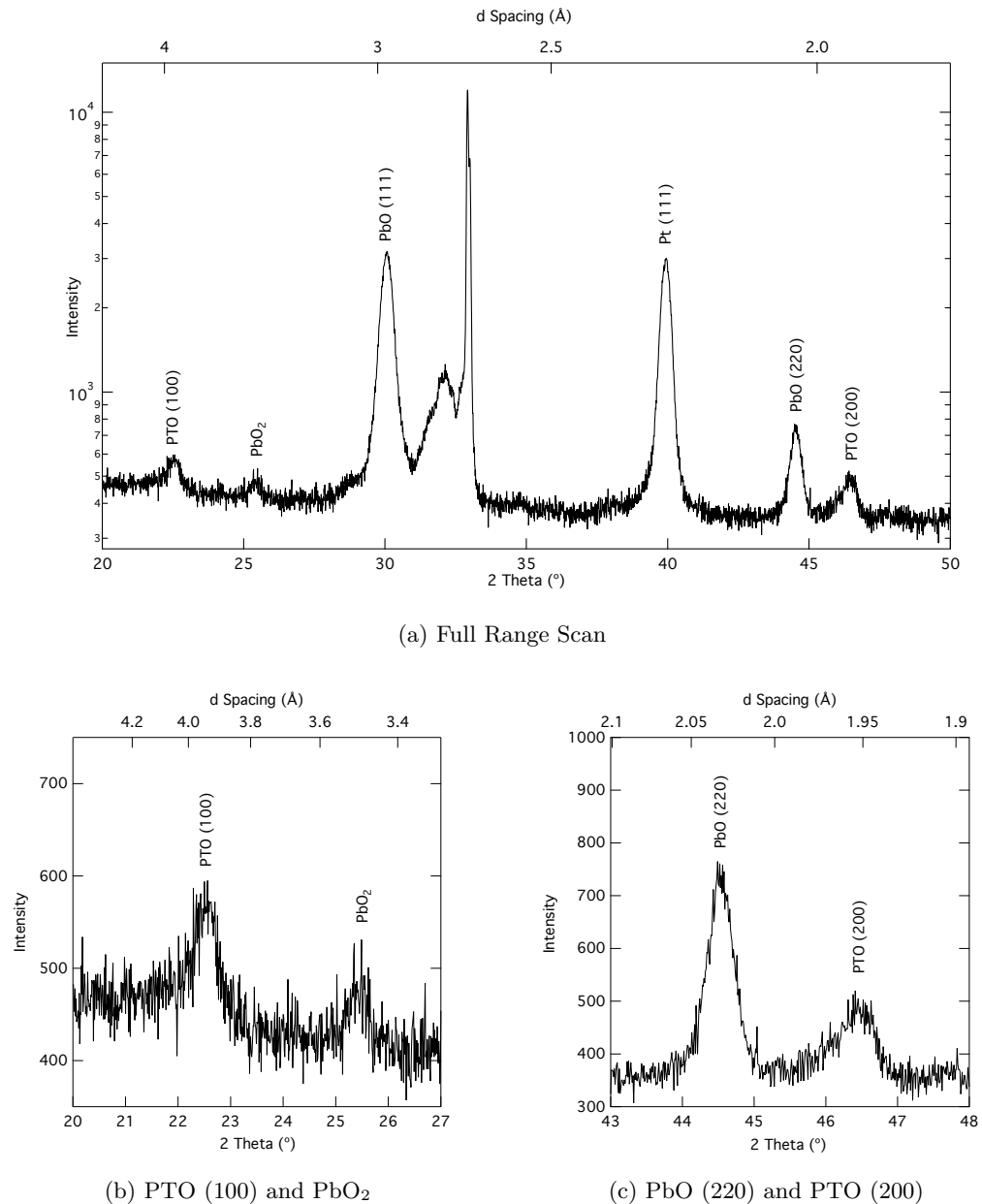


Figure A.14: XRD of #20 Pt